Published for the International Glaciological Society

IGS

THIS MANUSCRIPT HAS BEEN SUBMITTED TO THE JOURNAL OF GLACIOLOGY AND HAS NOT BEEN PEER-REVIEWED.

Crevasse locations and meltwater delivery to the bed in Pakitsoq, Greenland: Results from MimiNet, a new deep-learning model for crevasse detection

Journal:	*Journal of Glaciology*
Manuscript ID	JOG-2025-0095
Manuscript Type:	Article
Date Submitted by the Author:	03-Jul-2025
Complete List of Authors:	Khan, Naureen; University at Buffalo, Geology Poinar, Kristin; University at Buffalo, Earth Sciences Briner, Jason; University at Buffalo, Geology Crooks Nowicki, Sophie; University at Buffalo, Geology Mejia, Jessica; Syracuse University, Department of Earth and Environmental Sciences Verné, Mary; University at Buffalo, Geology
Keywords:	Crevasses, Remote sensing, Glacier hydrology
Abstract:	If surface crevasse fields deliver meltwater to the bed of the Greenland Ice Sheet, it would affect seasonal ice flow speeds and total mass balance. Whether they do is not currently known; some evidence suggests so, while specific field data suggest not. To address this gap, we develop MimiNet, a neural-network-based tool that identifies surface crevasse fields. We train MimiNet on Sentinel-1 scenes across a 629 km^2 area in Pakitsoq, central-western Greenland, and use it to locate crevasse fields annually over 2015–2024. We find that the crevassed area varied from a minimum of 141±25 km^2 in 2019 to a maximum of 183±27 km^2 in 2016, with no overall trend over the ten-year study period. We find that seasonal ice flow speed anomalies in crevasse fields are significantly higher than those in moulin-drained areas in July, but that in all other months of the melt season there is no difference between the two

	regions. We therefore infer that crevasse fields in Pakitsoq deliver meltwater to the bed, but in a spatially isolated way that keeps the local subglacial drainage system in an inefficient state for the entire melt season, while surrounding moulin-drained areas transition in mid-summer to a more efficient state.

Crevasse locations and meltwater delivery to the bed in Pakitsoq, Greenland: Results from MimiNet, a new deep-learning model for crevasse detection

Naureen Khan[1], Kristin Poinar[1,2], Jason Briner[1], Sophie Nowicki[1,2], Jessica Mejia[1,3] and Mary Verné[1]

University at Buffalo, NY, Department of Earth Sciences[1], RENEW Institute[2], Syracuse University, NY, Department of Earth and Environmental Sciences[3]

Abstract

If surface crevasse fields deliver meltwater to the bed of the Greenland Ice Sheet, it would affect seasonal ice flow speeds and total mass balance. Whether they do is not currently known; some evidence suggests so, while specific field data suggest not. To address this gap, we develop MimiNet, a neural-network-based tool that identifies surface crevasse fields. We train MimiNet on Sentinel-1 scenes across a 629 km^2 area in Pakitsoq, central-western Greenland, and use it to locate crevasse fields annually over 2015–2024. We find that the crevassed area varied from a minimum of 141±25 km^2 in 2019 to a maximum of 183±27 km^2 in 2016, with no overall trend over the ten-year study period. We find that seasonal ice flow speed anomalies in crevasse fields are significantly higher than those in moulin-drained areas in July, but that in all other months of the melt season there is no difference between the two regions. We therefore infer that crevasse fields in Pakitsoq deliver meltwater to the bed, but in a spatially isolated way that keeps the local subglacial drainage system in an inefficient state for the entire melt season, while surrounding moulin-drained areas transition in mid-summer to a more efficient state.

1 Introduction

1.1 Surficial meltwater routing on the Greenland Ice Sheet

Since the 1970s, the Greenland Ice Sheet has contributed 13.7 mm to global mean sea level rise, an average of 3.4 mm per decade (Mouginot and others, 2019). This mass loss has primarily occurred through ice discharge (calving) and surface meltwater runoff (Van Den Broeke and others, 2016). Runoff produced in the ice sheet ablation zone flows downslope in supraglacial streams and rivers with some 80% of this runoff flowing into moulins which deliver this water directly to the bed (Smith and others, 2015). The remainder is stored supraglacially, in wet snow or lakes, or englacially within surface crevasses (Smith and others, 2015).

Surface crevasses are fractures that form from deviatoric stresses as ice flows over an irregular bed or through a constriction (Colgan and others, 2016). Meltwater can drive the deepening of crevasses through hydrofracture; if there is sufficient water volume, crevasses can fracture hundreds of meters or more down to the ice-sheet bed (Das and others, 2008; Krawczynski and others, 2009). These crevasses can then maintain a direct hydraulic connection for meltwater from the ice sheet surface to the ice sheet bed (Hooke, 1989). Consistent meltwater input through these fully-propagated crevasses can form moulins, which are near-vertical tunnel-like features that carry meltwater to the basal environment (Alley and others, 2005; Das and others, 2008).

Once in the basal environment, surface meltwater can affect the state of the subglacial drainage system (Bartholomew and others, 2010; Van de Wal and others, 2015; Nienow and others, 2017). During the early part of the melt season, surface meltwater inputs increase the water pressure in the subglacial system, increasing basal lubrication that speeds basal sliding velocities (Bartholomew and others, 2010). Later in the melt season, sustained meltwater inputs can develop a channelized or efficient subglacial drainage system (Flowers, 2014). This decreases the overall water pressure and slows basal sliding velocities, allowing additional meltwater to enter the subglacial system without exceeding the hydraulic capacity of the channels or increasing sliding velocities (Schoof, 2010). Thus, surface meltwater input locations are important drivers of the spatial organization of subglacial channelization (Gulley and others, 2012; Mejia and others, 2022).

Crevasses require substantial meltwater input to form surface-to-bed connections (Krawczynski and others, 2009). When they lack meltwater input, crevasses typically propagate only tens of meters deep (Nye, 1955). The depth of a typical crevasse can vary with meltwater input. Field-informed studies from Pakitsoq, central western Greenland suggest that crevasses there transport supraglacial meltwater several hundred meters deep into the englacial system, where it can persist in liquid form for decades (Poinar and others, 2016) and eventually refreeze, warming the surrounding ice by several degrees (Phillips and others, 2010; Luthi and others, 2015). These observations suggest that these crevasses do not deliver meltwater to the bed, which was hundreds of meters below the maximum depth of the arrested crevasses. On the other hand, an early theoretical study found that a substantial volume of meltwater can propagate crevasses to the bed through hydrofracture (Alley and others, 2005). Ensuing theoretical and field studies found evidence in support of this, where water input from large supraglacial lake drainage events filled crevasses sufficiently to hydrofracture to the bed (Krawczynski and others, 2009; Das and others, 2008). Field studies away from supraglacial lakes have found evidence that water-filled crevasses propagate hundreds of meters deep into the ice sheet but arrest before reaching the bed (Luthi and others, 2015; Poinar and others, 2016). All these observations together suggest that crevasses serve as drainage pathways for meltwater to exit the supraglacial drainage system (Koziol and others, 2017), but whether they carry that water to the bed or retain it englacially is not generally known. McGrath and others (2011) used field data and modeling to find that crevasse fields drain about 48% of the surface meltwater runoff to the bed. This may vary across different crevasses, crevasse fields, regions, or across seasons.

As surface velocity patterns vary over time, it will change the spatial distribution of crevasses (Koziol and Arnold, 2018) and their role in delivering meltwater to the bed. A previous study found a substantial expansion of crevassed area extent in Pakitsoq between 1985 and 2009 (Colgan and others, 2011) while a recent study has found that crevassed area reduced between 2016 and 2021 in central western Greenland (Chudley and others, 2025). This suggests that there is substantial variability in the crevassed extent from decade to decade, but it is not known how quickly changes in crevassed area can take place, what the year-to-year variability in crevassed area may be, nor anything about the crevasse evolution in the intervening years between these two study periods. Here we develop an automated method to detect crevasse fields from satellite imagery and apply it to Pakitsoq, central western Greenland, over 2015–2024, in order to measure the trend and interannual variability in the crevassed area extent. We also analyze the seasonal evolution of ice flow velocity across crevassed and moulin-drained areas to test the hypothesis that crevasses in Pakitsoq carry meltwater to the bed, versus storing it englacially without delivering it to the bed.

2. Background

2.1 Existing methods for crevasse detection

The study of crevasses on ice sheets has a long history. For many decades, field crews have performed crevasse detection on ice sheets for the safety of ground-based research teams (Cook, 1956; Pings, 1961; Taurisano and others, 2006; Eder and others, 2008). Ground penetrating radar (GPR) is the most common on-site method. The radar waves can penetrate through the snow layers to several tens to hundreds of meters depth, depending on wavelength (Eder and others, 2008). Previous studies have collected and analyzed GPR data at study areas across a range of scales, including 1.8 km^2 (Ravanel and others, 2022), 3 km^2 (Kaluzienski and others, 2019), and 25 km^2 (Walker and others, 2019). Using GPR carried by helicopter, Thompson and others (2020) surveyed a 296 km^2 area. Assessing areas larger than this, however, requires a remote-sensing approach. Remote sensing allows features indicative of crevasses to be detected across wide areas, facilitating larger-scale hazard mapping (Colgan and others, 2011; Koike and others, 2012; Chudley and others, 2021; Herzfeld and others, 2021; Marsh and others, 2021; Libert and others, 2022). To date, these indicative features have included straight lines in visible imagery, bright places in radar imagery, or trenches in DEMs (Colgan and others, 2011; Marsh and others, 2021; Chudley and others, 2021) that have been detected manually by individual users, or algorithmically in an automated way. Manual analysis of remote sensing data (e.g., Colgan and others, 2011; Hoffman and others, 2018) is a time-consuming endeavor. Automated analyses of remote sensing imagery offer significant advantages. Recently, deep learning techniques have evolved, which enable data analysis over very large spatial scales, enabling a comprehensive dataset of crevasse distribution and ice sheet dynamics across the entire Antarctic Ice Sheet (Lai and others, 2020, Zhao and others, 2022, Surawy-Stepney and others, 2023). However, applying deep learning to detect crevasses from remote sensing imagery over the Greenland Ice Sheet has not yet been done. This is in part because of the difficulty of differentiating crevasses from other surface features, such as meltwater streams and lakes, which are prevalent in the Greenland ablation zone but rare across most of Antarctica. These distractor features are similar in scale (widths on the order of meters) to Greenland crevasses, which are substantially smaller and thus more difficult to resolve than Antarctic rifts and crevasses (widths on the order of hundreds of meters). This work aims to address this challenge by developing an automated crevasse detection method for the Greenland Ice Sheet using remote sensing over a 629 km^2 area of Pakitsoq (Fig. 1a), a historically well-studied region in central western Greenland.

2.2 Crevasse detection using Sentinel-1 SAR imagery

The Sentinel-1 satellite constellation carries Synthetic Aperture Radar (SAR) instruments that transmit C-band microwaves at 5.3 GHz frequency toward a surface, then receive back the reflected microwave signal (European Space Agency, 2014). In areas where the ice surface is smooth, SAR microwaves reflect a small portion of the microwave energy back to the receiver, making the surface appear dark in the produced image. Where the surface is rough, backscatter is higher, making the terrain appear brighter. SAR data thus provides a clear contrast between crevasse fields and non-crevassed ice, as rough crevasse fields appear bright and smooth ice surfaces appear dark in SAR imagery. The spatial resolution of Sentinel-1 SAR imagery is 10 meters, which is larger than the typical width of an individual crevasse (~5 meters). A pixel that overlaps a crevasse should therefore appear somewhat brighter than its surroundings, although not as bright as if a crevasse occupied the entirety of the pixel. However, due to the long length of most crevasses (at least a few hundred meters, shown in Fig. 1b–c), a single crevasse appears in Sentinel-1 SAR as a continuous line of brighter-than-average pixels. Furthermore, crevasses often cluster together in crevasse fields, which appear as bright patches with a distinct linear pattern (Fig. 1c).

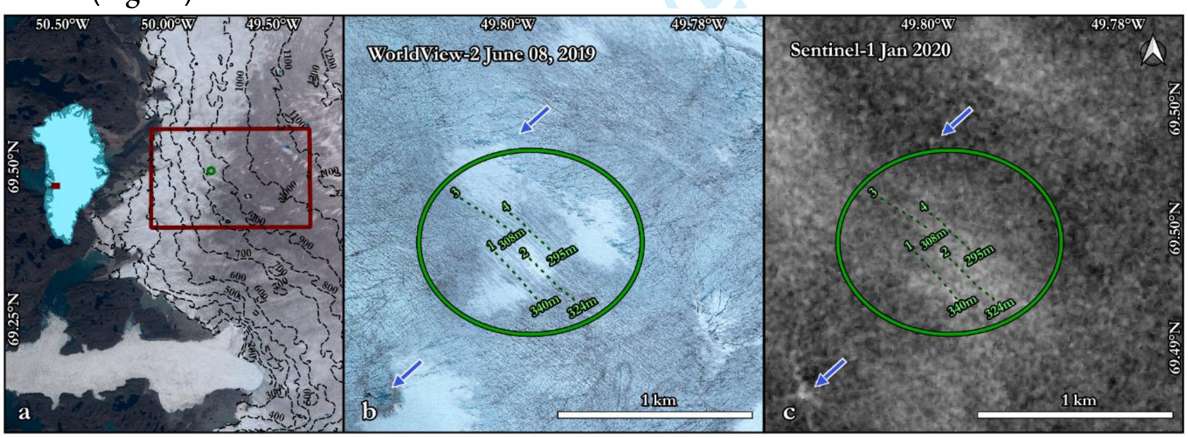

Figure 1: a) Sentinel-2 RGB image from August 2019 median showing our 629 km^2 study area of Pakitsoq, central-western Greenland, within the red box, overlaid by 100m surface elevation contours from BedMachine v5. Green circle shows the crevasse field in panels b and c. b) WorldView-2 imagery acquired June 08, 2019 (2.2 km × 2.2 km) showing a crevasse field in green circle. Green dashed lines denote four specific crevasses visible in this crevasse field, labeled with their corresponding lengths. Blue arrows indicate supraglacial drainage features near this crevasse field. c) Median of all Sentinel-1 SAR Level-1 Ground Range Detected HH single co-polarization scenes acquired in January 2020 (2.2 km × 2.2

km) showing the same crevasse field visible as a bright patch (green circle) with the four individual crevasses (green lines) discernible as thin linear features. Blue arrows again mark the two water features which appear as bright non-linear features.

Alternative remote-sensing data sources that resolve crevasses include optical image data from the European Space Agency's Sentinel-2 satellite constellation (10-meter multispectral spatial resolution), commercial WorldView-1 and WorldView-2 satellites (0.5-meter panchromatic and 2-meter multispectral spatial resolution, respectively), and NASA / USGS's Landsat-8/9 satellite constellation (15-meter panchromatic and 30-meter multispectral spatial resolution). In all of these sources, even in the highest-resolution WorldView-1 data, some crevasses and crevasse fields are not visible due to snow cover, cloud cover or daylight conditions. These problems are not faced by Sentinel-1, whose C-band SAR can penetrate the dry snowpack to a maximum depth of ~9 meters, and typically a few meters in our study area (Rignot and others, 2001). This makes Sentinel-1 imagery a very suitable dataset for detecting crevasses.

Crevasses at a perpendicular direction to the SAR incidence angle scatter back higher energy off the crevasse edge or wall facing the sensor, producing a bright surface return (Fig. 2). On the other hand, crevasses encountered at a parallel direction do not face the backscatter-enhancing wall and thus undergo higher forward scattering, producing a darker surface return (Marsh and others, 2021).

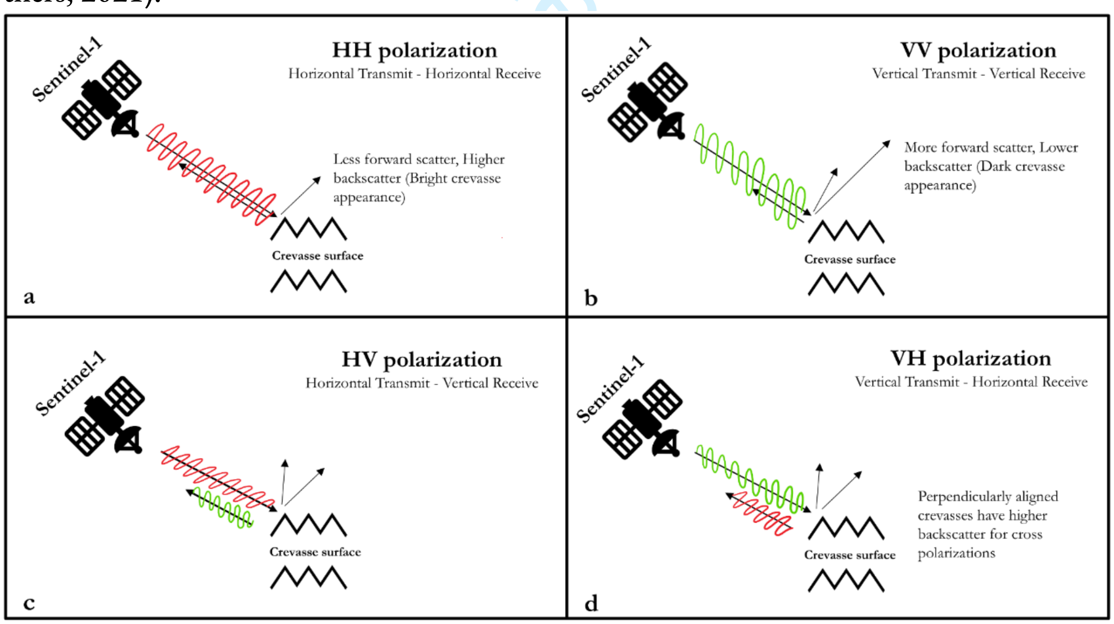

Figure 2: Sentinel-1 SAR polarization on crevasse surface: a) HH single co-polarization mode transmits and receives horizontally polarized microwaves. The HH mode is sensitive to surface slope, so crevasses create high backscatter and low forward scatter, producing a bright return in crevassed areas. b) VV single co-polarization mode transmits and receives vertically polarized microwaves. The VV mode is sensitive to surface roughness, so crevasses cause low backscatter and high forward scatter. This creates dark returns in crevassed areas. c and d) HV and VH cross-polarization modes combine some of the features of the co-polarization (HH and VV) modes, sometimes producing bright returns in crevassed areas but generally

returning lower energy overall. The cross-polarization modes produce contrast between crevassed and non-crevassed areas but suffer from higher energy loss.

Sentinel-1 SAR has four polarization modes: Horizontal Transmit and Horizontal Receive (HH) and Vertical Transmit and Vertical Receive (VV) single co-polarization, Horizontal Transmit and Vertical Receive (HV) and Vertical Transmit and Horizontal Receive (VH) dual band cross-polarization. Figure 2 illustrates the differences in backscatter among these modes. HH single co-polarization mode transmits and receives microwaves in the horizontal direction; when the transmit/receive orientation is perpendicular to the crevasse strike, the crevasse walls reflect back high scatter and consequently produce low forward-scatter. VV single co-polarization mode transmits and receives microwaves in the vertical direction. The vertically polarized waves are sensitive to surface roughness in any direction, so crevassed surfaces, regardless of their strike, produce high forward-scatter, in contrast to smooth surfaces that reflect higher scatter. This makes crevasses appear dark and smooth surfaces appear bright in VV polarization. Finally, HV and VH dual band cross-polarization modes each use both the horizontal and vertical directions. The vertical portion of HV and VH polarization produces forward-scattering or double-bounce backscattering on crevasses, which makes them appear dark, while smooth surfaces appear bright. Both HV and VH polarization modes yield high contrast between crevassed and non-crevassed areas (Marsh and others, 2021). However, the cross-polarization modes produce lower backscatter overall compared to the like-polarization modes, making dimmer images that have an overall less separable signal between crevassed and smooth areas. Therefore, we judge the HH single co-polarization SAR mode to work best for crevasse field detection in our application because it tends to generate bright observations with good contrast between crevasse fields and uncrevassed ice, and because it reduces noise when a double bounce backscattering occurs.

SAR backscatter from the Sentinel-1 satellite is sensitive to the presence of water in ice and snow. Thus, during the melt season when the surface is wet, water will absorb some microwave radiation, making the ice-sheet surface appear darker in the SAR imagery than at other times of year (Marin and others, 2020). This makes crevasse detection using SAR imagery more difficult, as there are lower returns from all surfaces, including crevassed areas. Therefore, we judge that winter seasons, when the surface is dry and therefore has low absorption of microwave radiation, are optimal for detecting crevasse fields.

2.3 Crevasse detection using deep learning

Deep learning models comprise multiple layers of neural networks that extract information from input data. We use convolutional neural networks (CNNs), an object-based detection method that detects features from input images using supervised classification (LeCun and others, 2015). Supervised classification requires that each input image be labeled or classified; the CNN ingests the labels to learn patterns inherent in the target features (Long and others, 2015). CNNs comprise interconnected nodes that are arranged in layers. Each node takes in inputs, processes them, and produces an output that it sends to the next layer of nodes (Buduma and others, 2022). The CNN assigns weights to the connections between the nodes, then modifies these weights during the training process to enhance the performance of the network against the known labels (Alzubaidi and others, 2021). Most image-processing CNNs are equipped with multiple convolution filters by which the models detect the target class from all features obtained through convolution (Gu and others, 2018). These convolution filters are small matrices that convolve across the image to find natural edges, lineations, or feature boundaries in the image (Zeiler and others, 2014).

Recent studies have harnessed the potential of CNN-based deep learning to identify crevasses on ice sheets in Antarctica (Lai and others, 2020; Zhao and others, 2022; Suraway-Stepney and others, 2023). However, no study yet has used CNNs for the identification of Greenland crevasses. The closest study is Chudley and others (2021), who applied a random forest classifier to elevation data over a small (7 km^2) field study area in western Greenland. While random forest classifiers are suitable for accurate crevasse detection within smaller datasets, they are not applicable for larger study areas, and do not leverage the convolution filters used in CNNs.

We use a CNN-based deep learning algorithm to extract patterns from Sentinel-1 SAR satellite imagery to detect crevasses at a regional scale. We use a modified version of the U-Net deep learning architecture with fully connected convolutional filters (Ronneberger and others, 2015). U-Net improves upon the base CNN algorithm by upsampling the extracted features into the same (or similar) pixel resolution and orientation as the original input image. Thus, the U-Net model not only detects target features in an image but also identifies their spatial locations. U-Net is designed to locate specific user-defined classes within an image by analyzing the image at multiple different scales. U-Net has been previously used for detecting glacier calving fronts in Greenland (Baumhoer and others, 2019; Mohajerani and others, 2019; Cheng and others, 2021). It has also been implemented for detecting crevasses on Antarctic ice shelves (Lai and others, 2020; Zhao and others, 2022; Surawy-Stepney and others, 2023). For example, Surawy-Stepney and others (2023) used a shallow layered U-Net to detect large (~200-meter width) crevasses on ice shelves and smaller (~50-meter width) crevasses on grounded ice; the latter is similar to the surface crevasses we target in Greenland. Their results suggest that small crevasses are significantly more difficult to identify than large crevasses. We address this challenge by developing a new model based on U-Net to detect densely spaced, narrow crevasses on the Greenland Ice Sheet.

3 Methods

3.1 Study area and remote sensing data

Our study area encompasses a ~30 × 20 km^2 area of the Pakitsoq region in central western Greenland, centered at 69.47°N, 49.72°W. This region has a long history of glaciological studies (Thomsen and others, 1989; Colgan and others, 2011; Andrews and others, 2014; Luthi and others, 2015; Koziol and others, 2017; Mejia and others, 2022). Particularly, Hoffman and others (2018) used WorldView-2 satellite imagery to manually digitize the locations of crevasse fields in a subset of our study area over 2009–2011, making a valuable independent comparison dataset.

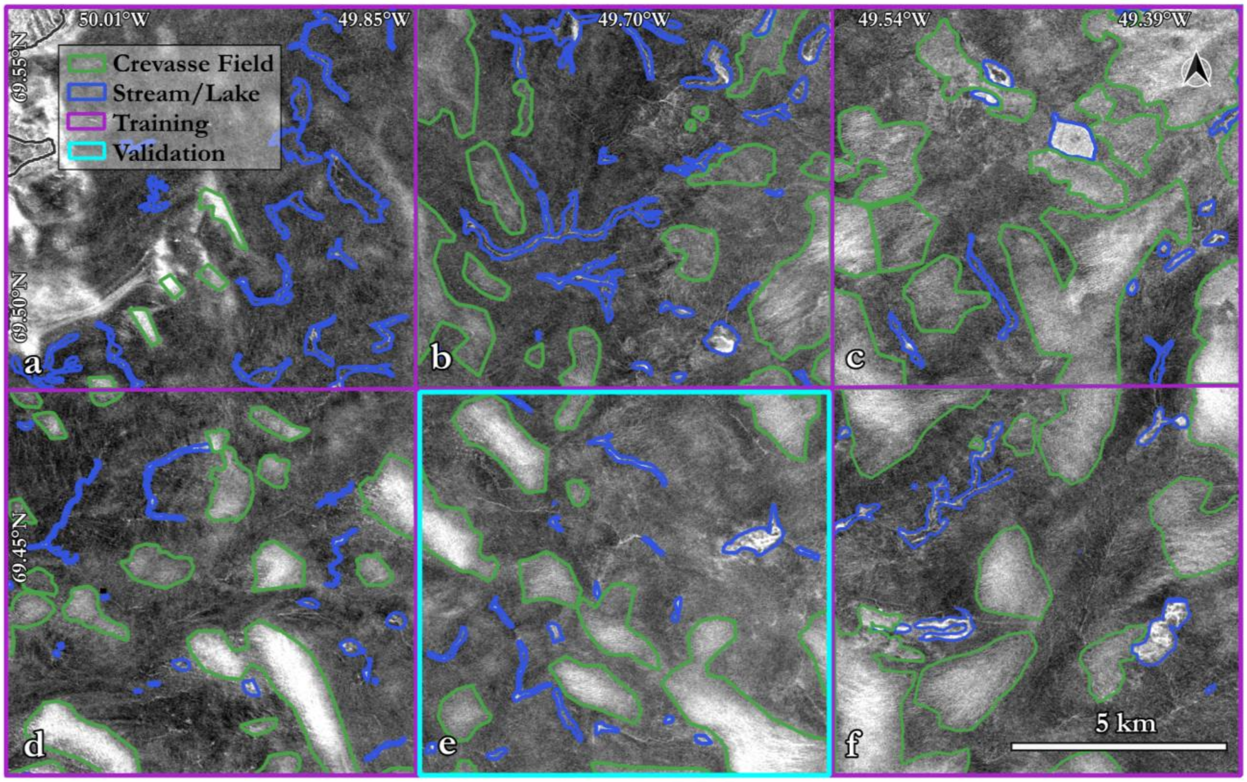

Figure 3: Study area, a 30.72 km × 20.48 km area of Pakitsoq shown in Fig. 1a. We divide this area into regions A–F. Region A shows 15m ice sheet margin black outlines from GIMP ice mask. We use the median of all Sentinel-1 SAR Level-1 GRD HH single co-polarization scenes acquired in January 2020 for training the model. Manually digitized ground truth labels containing crevasse field (green polygons) and stream/lake (blue polygons) are used as training (purple boxes) and validation (cyan box) datasets.

We constructed and analyzed a representative wintertime scene from Sentinel-1 SAR Level-1 Ground Range Detected (GRD) imagery covering 30.72 km × 20.48 km in Pakitsoq. We constructed this scene from 17 individual Sentinel-1 scenes, acquired on January 1, 3, 4, 7–10, 13, 15, 16, 19–22, 25, 27 and 28 of 2020, which we accessed using Google Earth Engine (Gorelick and others, 2017). Google Earth Engine pre-processes Sentinel-1 SAR raw scenes using the Sentinel-1 Toolbox, which applies thermal noise removal, radiometric calibration to convert radar backscatter coefficient in decibels using log-scaling for normalization, and terrain correction to orthorectify the scenes (Veci and others, 2017). We selected the HH single co-polarization and interferometric swath mode, generated their pixel-by-pixel median over the 17 acquisition dates, and exported the resultant median scene as a 64-bit GeoTiff raster with the native 10-meter spatial resolution. To gain compatibility with U-Net, we converted this raster to an 8-bit image using the LZW Lossless Image Compression method in QGIS. We divided our study area into six regions, each 10.24 km × 10.24 km (Fig. 3) and allocated them as training and testing (regions A, B, C, D, and F) and validation (region E) datasets. We next subdivided each region raster into four tiles (5.12 km × 5.12 km each) to reduce computational runtime and maintain compatibility with U-Net, which expects 512 × 512 pixel inputs. Thus, six regions divided into four tiles yielded 24 tiles each of 512 × 512 pixels; we used 20 tiles as the training and testing data and 4 tiles as the validation data. We chose region E to be the validation dataset as it has a mix of crevasse fields, supraglacial streams, and lakes.

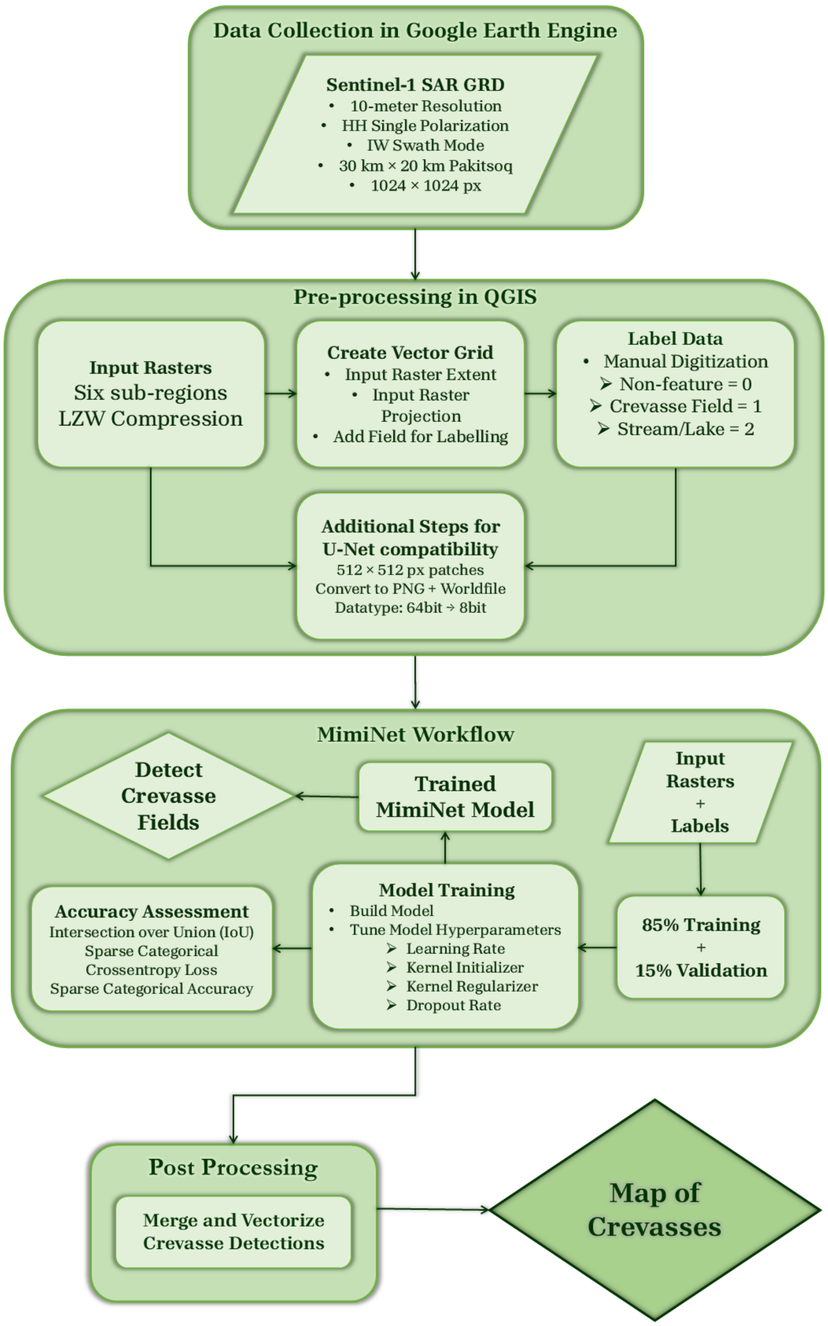

Figure 4: Automated crevasse detection workflow. From the top down: Data collection in Google Earth Engine: export Sentinel-1 SAR imagery for Pakitsoq region with outlined parameters → Pre-processing in QGIS: change format of the exported rasters + ground truth labels → MimiNet workflow: input processed images and labels to train model + perform model hyperparameter tuning = Crevasse detection + metric scores → Post-processing: merge and vectorize all crevasse field detections → Final output of map of crevasse fields.

3.2 MimiNet crevasse field detection

We developed MimiNet, a deep learning workflow that adapts U-Net to the specific problem of crevasse field detection on the Greenland Ice Sheet ablation area from Sentinel-1 SAR images. Like U-Net, MimiNet uses image segmentation, which is a pixel-based classification method that requires ground truth labels that identify target features in the training dataset. The primary target feature of MimiNet is crevasse fields, but these features are interspersed with the remnants of summertime meltwater features, such as supraglacial streams and supraglacial lake beds, which often appear similarly bright in Sentinel-1 SAR imagery (Surdu and others, 2014). To avoid conflating crevasse fields with these meltwater features, we trained the model to identify three classes: non-features (ice without crevasses or streams), crevasse fields, and supraglacial streams/lakes. We manually created training labels by outlining all features in the median of all Sentinel-1 scenes acquired over January 2020 across our study area (Section 3.1), using a screen ratio of 20000:1 and a digitization radius of 150–600 m (15–60 pixels in Sentinel-1 imagery) in QGIS. Figure 5 shows the processing chain: the input raster, the manually annotated vector shapefile, and finally the three categories of rasterized labels. Our three target classes are as follows: non-features (white regions), crevasse fields (green regions), and stream/lake (blue regions).

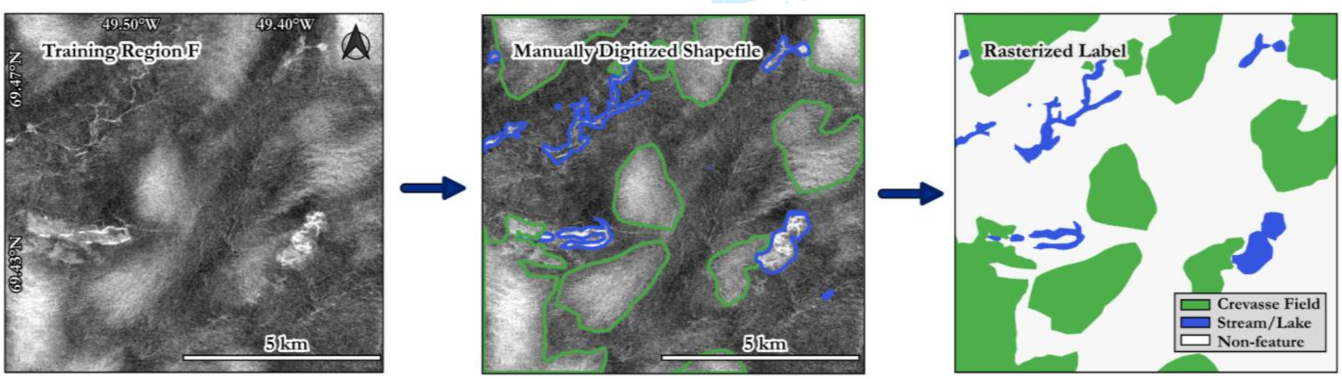

Figure 5: (From left to right) The median of all Sentinel-1 SAR Level-1 GRD HH single co-polarization scenes acquired in January 2020 over the training region F (1024 px × 1024 px) ⇒ Manually classified vector shapefile containing crevasse fields (green polygons) and stream/lake (blue polygons) ⇒ Rasterized labels containing three classes: non-features (class 0, white region), crevasse fields (class 1, green regions), and stream/lake (class 2, blue regions).

3.2.1 MimiNet model structure

We adapted the U-shaped U-Net Architecture to develop MimiNet, as shown in Figure 6. The left portion of Figure 6 shows the downsampling path and the right portion shows the upsampling path. MimiNet extracts features through three layers in the downsampling path. The inputs are 512 × 512 pixel single-band 8-bit images with pixel values from 0–255. In each layer, the image is processed through two 3 × 3 convolution filters and then one 2 × 2 max pooling filter. Each convolution filter (yellow arrow) convolves across the image to extract feature maps. In the first layer, the two convolution operations produce 16 extracted feature maps per image. In the second layer, the two convolution operators extract 32 feature maps, and 64 feature maps in the third layer. At the end of each layer along the downsampling path, a max pooling operator (pink arrow) takes the maximum pixel values across 2 × 2 windows, thereby reducing the spatial size by a factor of four (a factor of two in each direction), i.e, from 512 × 512 to 256 × 256 in the second layer, and from 256 × 256 to 128 × 128 in the third layer. Next, the 64 feature maps extracted at the third layer are upsampled to regain the spatial size lost along the downsampling path. A 2 × 2 upsampling filter (purple arrow) duplicates rows and columns of the image matrix, then the feature maps are cropped and concatenated with the feature maps from each downsampling layer. Two more 3 × 3 convolution filters are applied after every upsampling and then a final 1 × 1 convolution filter (also known as the activation function) is applied to reduce the image depth from 16 feature maps to the number of target classes (three), producing a 512 × 512 × 3 output image.

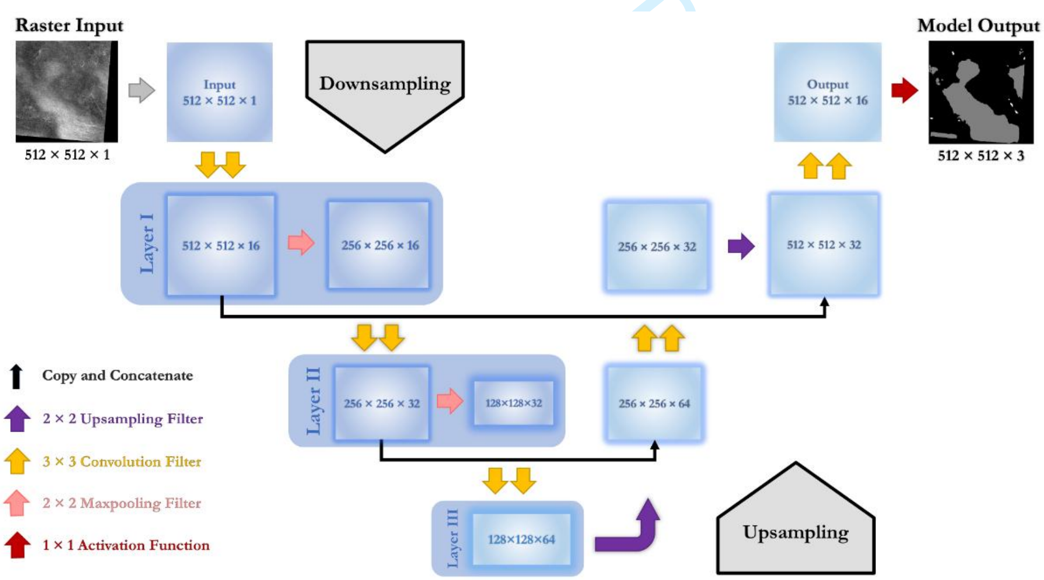

Figure 6: MimiNet model structure for detecting crevasses on the Greenland Ice Sheet. The downsampling and upsampling design its U-shaped architecture. Different arrows indicate the filters used in the model. The raster input is 512 pixels × 512 pixels from the median of all Sentinel-1 SAR Level-1 GRD HH single co-polarization scenes acquired in January 2020 (top-left) and the model output (top-right) contains detected crevasse fields (gray regions), supraglacial streams/lakes (white regions) and non-feature (black regions) class.

3.2.2 Ghub workflow implementation

We developed and ran MimiNet on Ghub, a gateway for datasets, analysis tools, and supercomputing resources for ice sheet science (Sperhac and others, 2021). We used the Ghub JupyterLab tool (Clark, 2023) for its functionality of opening terminal, console, and python editing modules as well as using multiple notebooks on one browser tab. We authenticated a GitHub repository to contain all files required for this project for managing version control during project development. We used Keras, an open-source deep learning library built with the Tensorflow machine learning framework (Abadi and others, 2016) and Tensorflow 2.15 (TensorFlow Developers, 2023) for our MimiNet model. We modified the Tensorflow version 2 based implementation of U-Net (Akeret and others, 2017) to ensure compatibility with our workflow.

3.2.3 Model training workflow

Supervised learning guidelines stipulate using ~85% of a labeled dataset to train the model and the remaining ~15% to validate the trained versions of the models (Moolayil and Moolayil, 2019). As our model requires Tensorflow Dataset structure input, we utilized the Tensorflow data API to build our model input pipeline. This creates an efficient dataset pipeline that saves computation time regardless of dataset size and increases preprocessing options. We built MimiNet around the U-net model structure, which requires definition of the expected input image size and number of channels, the number of target classes, the number of model layers, the number of feature maps in the first layer, the size of the convolution and max-pooling filters, the dropout rate, the type of padding used during image convolutions, and the type of activation function used for the final output.

We explored optimization of key parameters to achieve the best model performance output, which we judged by assessing the accuracy, loss, and Intersection over Union (IoU) score for both training and validation datasets. These evaluation metrics are the functional form of the calculation of loss (inaccuracy) between the labels and predictions. We varied the optimizer, dropout rate, initializer and regularizer to prevent model underfitting or overfitting. The optimizer function is used to converge the model quickly while preventing underfitting using the learning rate hyperparameter, which controls how fast the model adjusts its coefficients across subsequent iterations. We varied the learning rate from 0.0001 to 0.1, depending on the type of the optimizer. We assigned a rate to the dropout layer to randomly drop input units as the model adjusts weights between the nodes, which also helps prevent model overfitting. We tested dropout rates of 0 to 0.5. The kernel initializer and regularizer work together as the model adjusts weights during training for each layer. The initializer sets how to initialize weights whereas the regularizer adds a penalty in cases where the model over adjusts weights. We tested initializers known as Wendy, Ryan, and Bratwurst and varied the regularizer over 0.1 to 100.

We began model training by defining the training and validation dataset, the number of epochs, batch size, and all necessary callback functions. Each epoch refers to a complete pass of the whole dataset through the model; between epochs, model weightings are adjusted to produce a new version of the model. The batch size refers to the number of training files in a model forward and backward pass or the number of training files to be processed in a model run. We trained our model for 900 epochs with a batch size of one. We also used callback functions to track and monitor model training for every step, which can be utilized to stop model training as the model metrics stop improving. We used Tensorboard, a model parameter organization and visualization tool incorporated in Tensorflow Version 2, to visualize the model training progress at each iteration to define callback functions. Tensorboard displays the training performance at every step, shows what the model learned from the training samples, and plots the evaluation metrics.

*3.2.4 Model evaluatio*n

We evaluated our model outputs using accuracy, loss, and IoU across the training and validation datasets. Accuracy refers to the fraction of correct predictions (true positives and true negatives) while loss refers to the fraction of wrong predictions (false positives and false negatives). We measured accuracy using the Sparse Categorical Accuracy function to suit our three discrete, non-overlapping classes (Moolayil and Moolayil, 2019). We measured the training loss similarly, using the Sparse Categorical Cross Entropy function (Terven and others, 2024).

We used the IoU metric for evaluating the overall model performance. This is the most widely used evaluation metric for semantic image segmentation problems (Cheng and others, 2021; Zhang and others, 2021; Chu and others, 2022; Herrmann and others, 2023; Loebel and others, 2023). This metric is defined as follows:

$$IoU = \frac{TP}{TP + FP + FN} \quad \text{(Eq. 1)}$$

Here, true positives (TP) is the number of correctly predicted pixels that belong to a given class, false positives (FP) is the number of incorrectly predicted pixels for that class, and false negatives (FN) refers to the number of missed predictions for that class. Possible values of IoU range from 0 to 1, where 1 means the model achieved 100% correct detection and 0% errors. We used the jaccard similarity coefficient score metric from the scikit-learn open-source machine-learning library (Pedregosa and others, 2011) to calculate the IoU scores for each class in our model predictions as well as the mean IoU score across all three classes for evaluating the overall model performance.

The IoU provides a balanced metric by excluding the true negatives. For our application, this is advantageous because of the imbalanced classes: most of our pixels are in class 0 (non-features), whereas our scientific interest is in class 1 (crevasse fields). Thus, a poor-quality model could nevertheless achieve good accuracy by over-predicting class 0, equivalent to performing well at identifying featureless ice surfaces at the expense of identifying crevasse fields. We prevent this possibility by excluding true negatives in our evaluation metric (Equation 1), instead emphasizing true positives (correctly identified crevasse fields).

3.3 Analysis of crevasse extent in Pakitsoq over 2015–2024

We studied the changes in the total crevassed area in our study region by applying our automated crevasse detection workflow to summary images we generated from the Sentinel-1 HH single co-polarization images over 2015–2024. Specifically, we constructed pixel-by-pixel median images for all available imagery each spring, which we defined as January through April of each year in the ten-year period. This was because in all years except for 2020, we found that January medians of HH polarization contained a large amount of speckle noise, which interferes with accurate crevasse field detection. Therefore, we expanded the time range over which we took the median to maximize speckle removal while still remaining within the winter season to avoid any meltwater presence. We used manually digitized crevasse field shapefiles from Hoffman and others (2018), which cover three years (2009, 2010, and 2011), to extend the study of the total crevassed area in Pakitsoq farther back in time.

3.4 Uncertainty in crevassed area

We used the six models whose hyperparameter combinations are shown in Table 1 to calculate the uncertainty of the crevassed area in Pakitsoq over our study area. To do this, we trained all six models on Sentinel-1 HH single co-polarization of the January 2020 median imagery, but we varied the label datasets across these models. We trained five models on labels of crevasse fields digitized on this same Sentinel-1 image (Models 6, 7, 9, 16, and 17; Table S1). We trained the sixth model (also Model 6) on labels digitized based on WorldView-1 imagery acquired on July 9–10, August 11, 2015, and May 19, 2020. Different users generated the two label datasets, but each user followed the same rules (described in Section 3.2). We used these six trained models to calculate the standard error (SE) of the mean of the total and sub-regional crevassed area for every year in our ten-year study period, following:

$$SE = \frac{\sigma_{YM}}{\sqrt{N_M - 1}} \quad \text{(Eq. 2)}$$

where σ_{YM} refers to the yearly standard deviation of our six models (Models 6, 7, 9, 16, and 17 trained on Sentinel-1 based labels and Model 6 trained on WorldView-2 based labels) and N_M = 6, the number of models. The quantity $N_M - 1$ refers to the degree of freedom of N_M.

3.5 Summer ice flow speed

We analyzed the seasonal patterns of ice flow speed over our study area using 120-meter spatial resolution ITS_LIVE ice velocity data (Gardner and others, 2025) accessed through the open-source ITS_LIVE x-array tutorial (Marshall and others, 2022) over the period 2015–2024. We investigated the summer velocity anomalies compared to the temporal mean of both moulin-drained and crevassed areas and the associated speedup and slowdown pattern between them in the study area persistent throughout 2015–2024. To do so, we defined crevasse fields as areas with crevasse detections at least 8 out of 10 years and moulin-drained areas as those with non-feature, supraglacial stream and lake detections at least 8 out of 10 years. We also divided our study area into three elevation zones: lower elevation (approx. 500–750 meters), mid elevation (approx. 750–950 meters) and higher elevation (approx. 950–1100 meters) to study the spatial and temporal pattern of speedup and slowdown through the melt season.

We implemented strict filtering criteria to ensure data quality in ice velocity observations. The ITS_LIVE ice velocity dataset presents the observation date as the midpoint of the two acquisition dates of satellite image-pairs. We required a maximum time separation of 15 days for each image pair, ensuring that each data point reflects an average ice-flow speed over a short time period. We also discarded velocity observations with an error exceeding half of the velocity magnitude. We next resampled the filtered velocity observations to 15-day intervals and then linearly interpolated these to daily observations. We used the following equation to calculate the individual monthly velocity anomalies of both moulin-drained and crevassed areas:

$$V'(x, y, t) = V(x, y, t) - \mu(x, y) \qquad \text{(Eq. 3)}$$

Here, $V'(x, y, t)$ is the velocity anomaly at each spatial point and time, $V(x, y, t)$ is the individual velocity of each spatial point and time, and $\mu(x, y)$ is the mean velocity of each spatial point through 2015–2024. We then calculated the mean velocity anomalies for each month across all years for both moulin-drained and crevassed areas.

Finally, to analyze the difference in seasonal velocity patterns across the two areas, we calculated the Z-scores of crevassed areas versus moulin-drained areas for each calendar month. We used the following equation for the Z-scores:

$$Z = \frac{\mu_{v'c} - \mu_{v'nc}}{\sqrt{\frac{\sigma^2_{v'c}}{N_{v'c}} + \frac{\sigma^2_{v'nc}}{N_{v'nc}}}} \qquad \text{(Eq. 4)}$$

Here, $\mu_{v'c}$ and $\mu_{v'nc}$ are the mean velocity anomalies of crevassed areas and moulin-drained areas, respectively, for a given calendar month over 2015–2024, $\sigma_{v'c}$ and $\sigma_{v'nc}$ are the respective standard deviations, and $N_{v'c}$ and $N_{v'nc}$ are the respective number of velocity anomaly observations in each calendar month. Values of $|Z| > 2.58$ indicate a significant difference in velocity anomalies between crevassed and moulin-drained areas at 99% confidence. Positive Z-scores denote crevassed areas experiencing higher velocity anomalies than moulin-drained areas while negative Z-scores denote moulin-drained areas experiencing higher velocity anomalies than crevassed areas.

4 Results

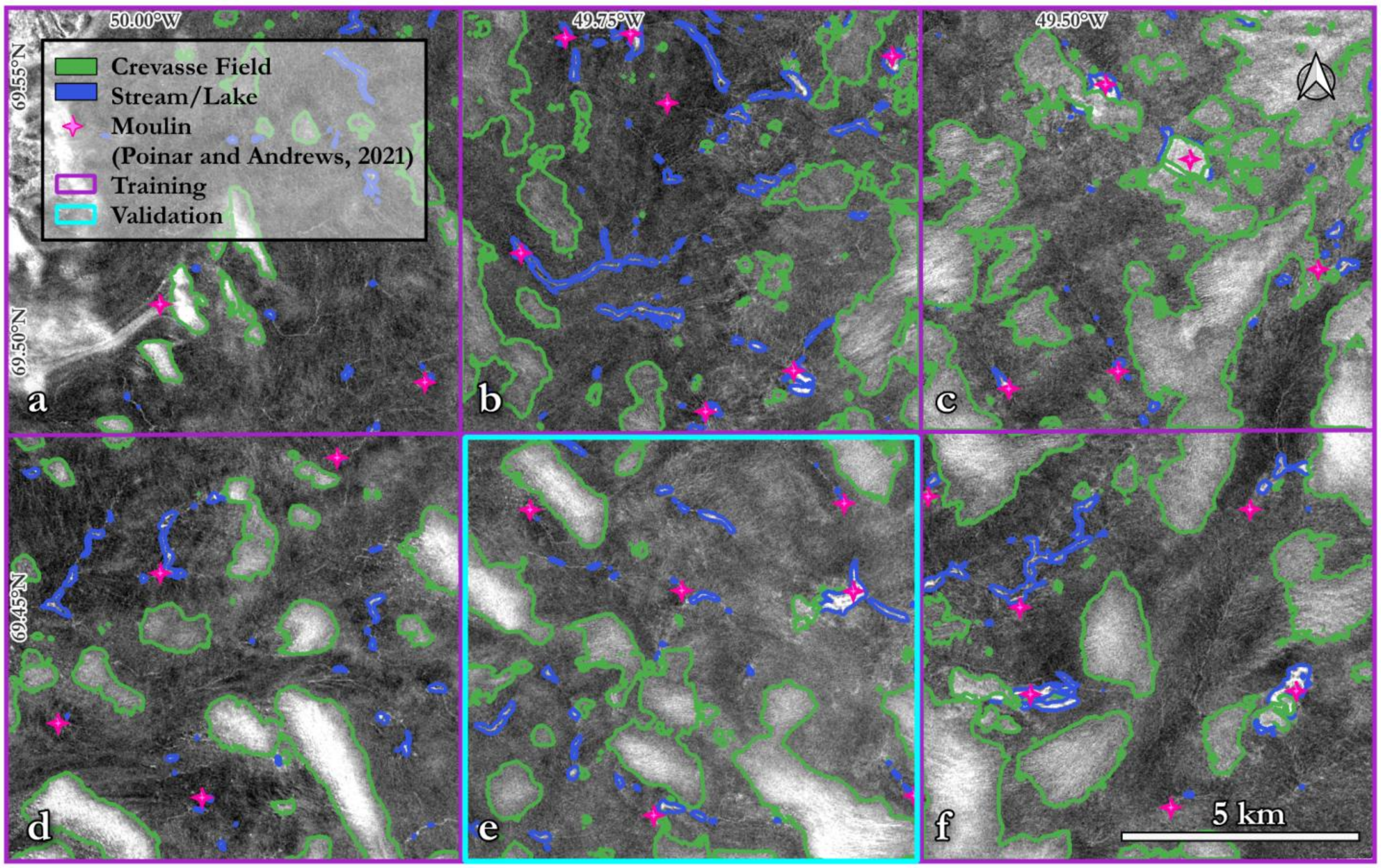

Figure 9: Model 6 (Table S1) detected crevasse field (green) and stream/lake (blue) shapefiles overlain on the entire Pakitsoq training region (divided into regions a–f). Purple boxes represent the training dataset of twenty subregions used to train the MimiNet model. Cyan box shows the validation dataset of four subregions used to validate model training at every epoch. Pink stars represent moulin locations over 2009–2019 identified by Poinar and Andrews

(2021).

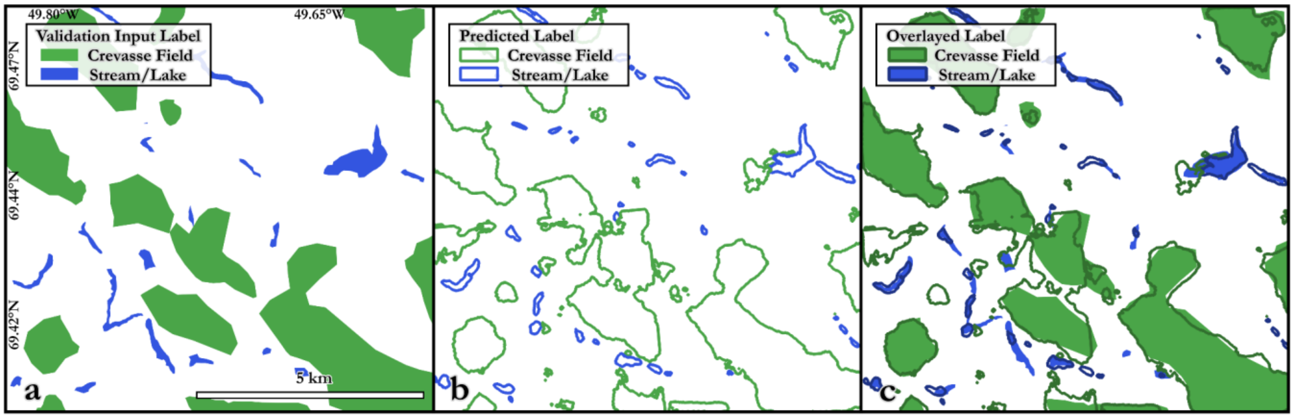

Figure 10: a) Manually classified labels of crevasse fields (green filled-polygons) and streams/lakes (blue filled-polygons) in region E of our study area. b) Model predicted crevasse fields (green outlined-polygons) and streams/lakes (blue outlined-polygons) in region E of our study area. c) Both the manually classified labels and the model predictions in region E are shown together.

Figure 9 shows the output of Model 6 for the presence of crevasse fields (green) and supraglacial streams and lakes (blue) in the winter of 2020. Model 6 scored 91% training accuracy, 24% training loss, 83% training mean IoU, and 75% training IoU on crevassed areas at the final epoch of training. On validation data (cyan box, Fig. 9e), the model scored 93% validation accuracy, 19% validation loss, 87% validation mean IoU, and 75% validation IoU on crevassed areas. These output metrics are listed in Table S1. Figure 10 shows the manually classified and model-predicted crevasse fields and supraglacial streams and lakes from validation region E in our study area.

After training and validation, our model identified a total area of 152 ± 24 km^2 covered by crevasse fields in Pakitsoq in the winter of 2020. This represents 20% of the entire 629 km^2 study area. Most (55%) of the crevassed area lies in large crevasse fields (sized 3.5 km^2 or larger), whereas 45% of the crevassed area are in smaller regions. We found that region C, the highest-elevation area in the northeast quadrant of our study area, was the most heavily crevassed, with 40±5 km^2 of crevassed area (38% of its total 105 km^2 area). Remnant supraglacial streams and lake features identified in winter imagery accounted for a much smaller portion of the landscape, covering only 13±2 km^2, or just 2% of the total area.

We also display locations of 32 moulins identified over 2009–2019 by Poinar and Andrews (2021) in our study area. We found 30 of these previously identified moulins nearby our model-detected supraglacial streams and lake features, except one in region A next to a nunatak and one in region C on the edge of a crevasse field bordering with supraglacial features.

4.1 Temporal persistence of crevasse field locations

We present our detections of crevasse fields and supraglacial streams/lakes over 2015–2024 for region E in Figure 11a–j. To assess the temporal variability in crevasse field locations, we define a "persistent crevasse field" as a collection of pixels that our workflow identified as a crevasse field for at least 8 out of 10 years in the study period (Figures 11k and 12). We found that 60% of our study area was occupied by crevasse fields detected for two years or less. 36% of our study area had crevasses for at least 8 out of 10 years, and only 4% of our study area was variable with crevasses in 3 to 7 years. Essentially all the crevasse fields we detected tend to occupy the same areas throughout the 2015–2024 period studied.

We compared persistent crevasse fields with the crevasse fields detected by Hoffman and others (2018), which are outlined in yellow (Fig. 11k, 12). The Hoffman dataset contains 42 distinct crevasse fields, with a total crevassed area of 77 km^2. Of those 42 crevasse fields, 39 directly coincide with crevasse fields in our dataset. In 34 of those, our crevasse fields were larger than the ones in Hoffman and others (2018), while three were smaller. Region E contains the excluded two crevasse fields that Hoffman and others (2018) digitized according to their study area bounds. The Hoffman and others (2018) crevasse fields from 2009–2011 scored 70% mean IoU and 46% crevasse IoU against our persistent crevasse field dataset.

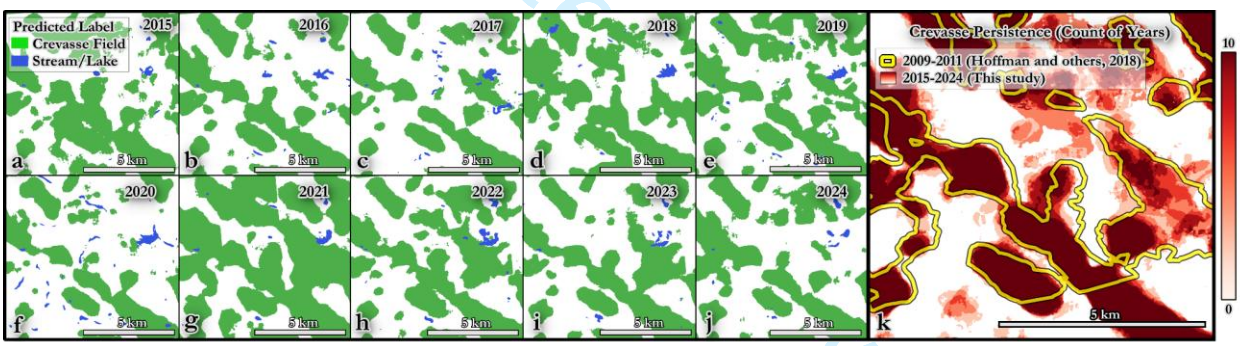

Figure 11: a-j) Model predictions of crevasse fields and supraglacial streams/lakes in region E from 2015–2024. k) Map of persistent crevasse field detections over the 10-year study period in region E. Red shading denotes the total number of detections over 2015–2024, with white meaning no detections and deep red meaning crevasse fields detected all 10 years. Yellow polygon outlines show crevasse fields detected by Hoffman and others (2018) in 2009–2011.

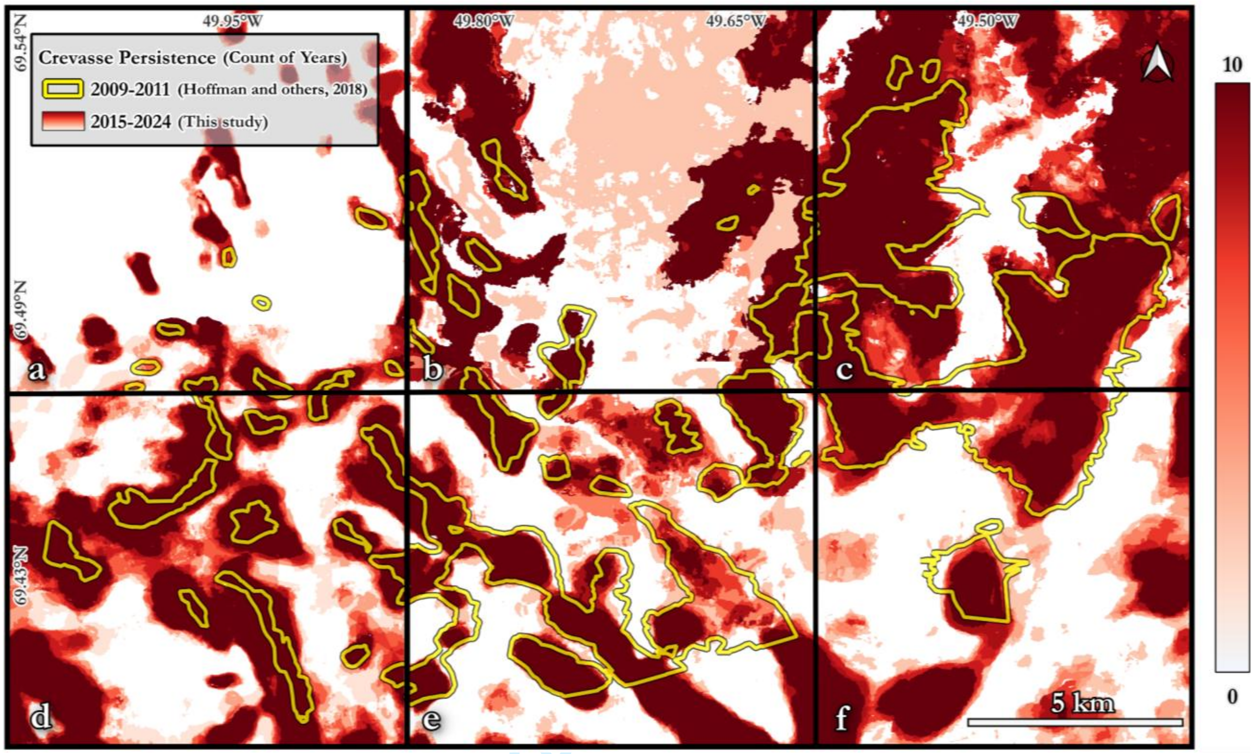

Figure 12: Map of persistence crevasse field detections over the 10-year study period on the entire Pakitsoq study area. Red shading denotes the total number of detections over 2015–2024, with white meaning no detections and deep red meaning crevasse fields detected all 10 years. Yellow polygons show crevasse fields detected by Hoffman and others (2018) in 2009–2011 for comparison.

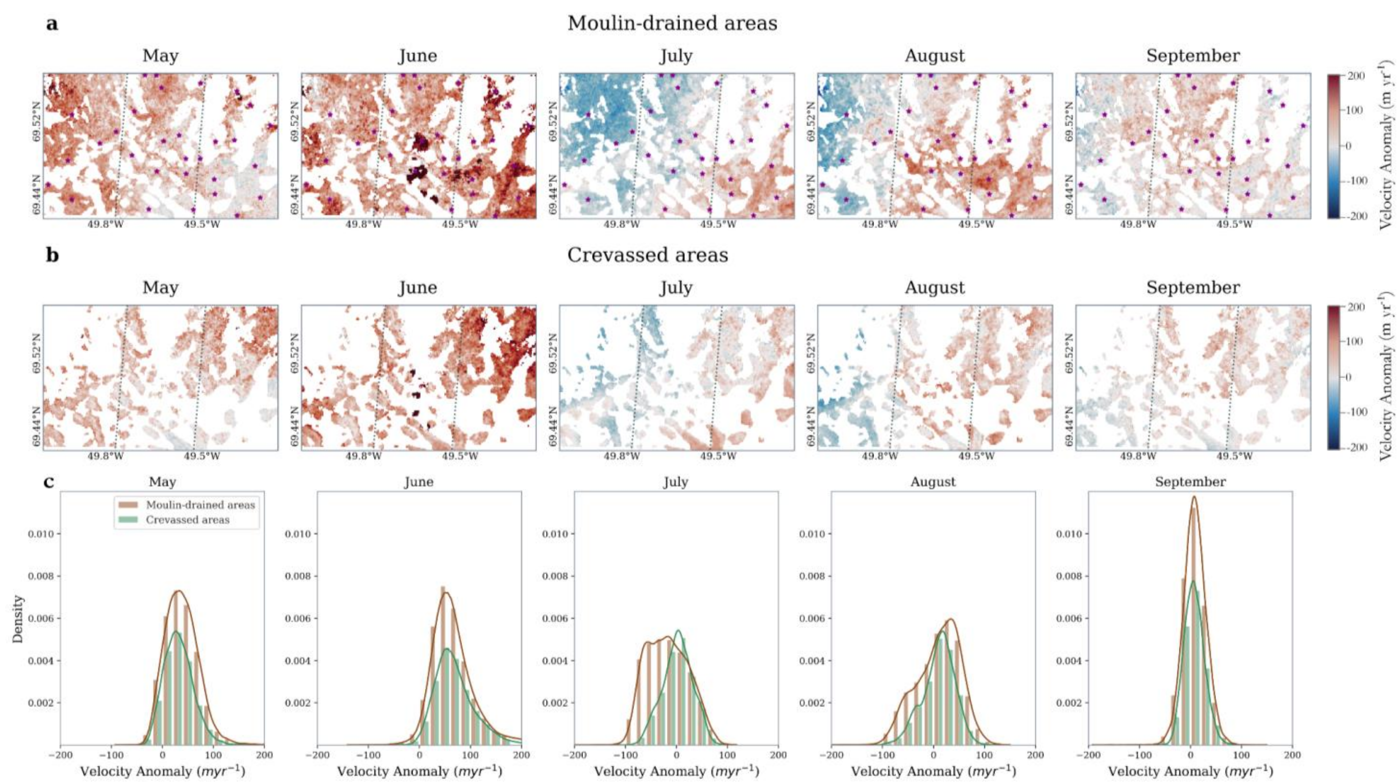

Figure 13: Monthly velocity anomalies of persistent a) moulin-drained and b) crevassed areas in the Pakitsoq study area, averaged over 2015–2024. Previously identified moulin locations (purple stars) from Poinar and Andrews (2021) are shown in panel a. Dotted lines show the three elevation zones (from left to right): lower-elevation (approx. 500–750 m), mid-elevation (approx. 750–950 m), and higher-elevation (approx. 950–1100 m). c) Histogram density plots of the monthly velocity anomalies of persistent moulin-drained (brown) and crevassed areas (green). Persistent moulin-drained and crevassed areas are defined as features detected over ≥8 of the 2015–2024 study period.

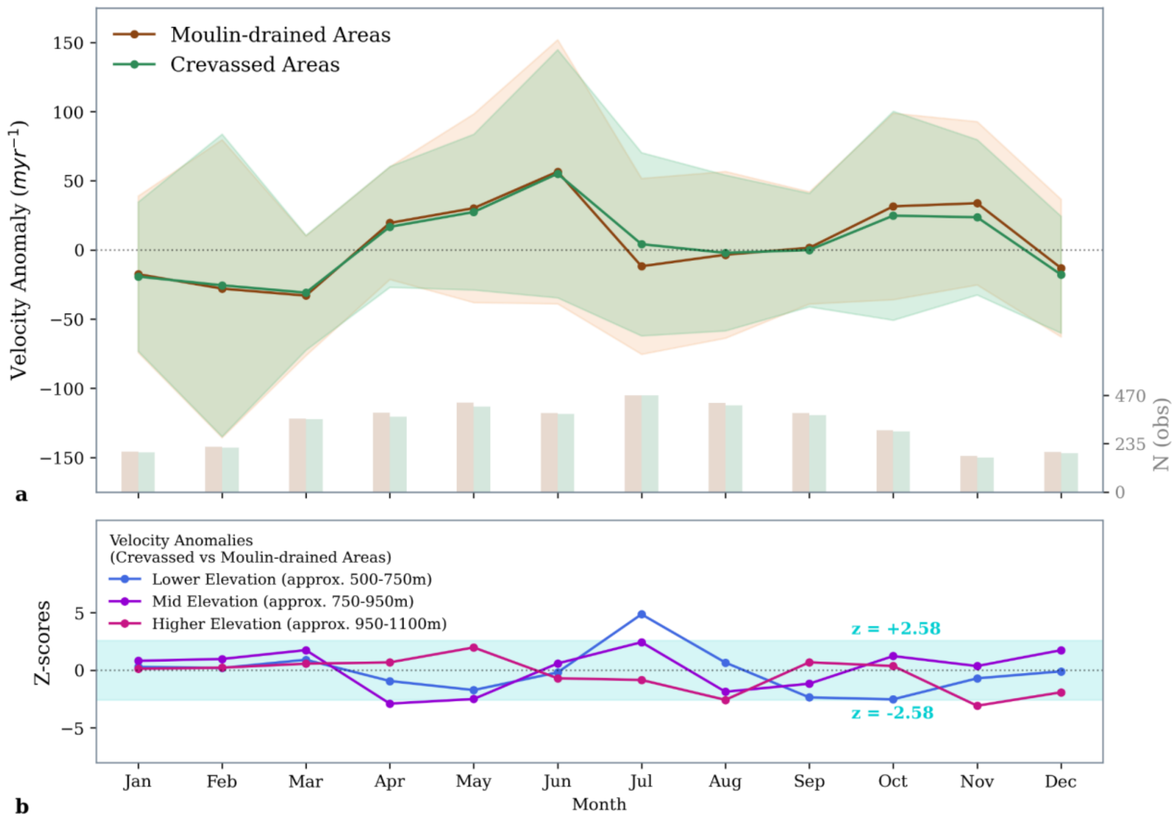

Figure 14: a) Velocity anomalies from 2015–2024 averaged over moulin-drained areas (brown) and crevassed areas (green) in Pakitsoq study area with 1σ error envelopes shown for January–December months. Number of ITS_LIVE velocity observations of moulin-drained (brown) and crevassed areas (green) for January–December months within velocity filtering criteria are shown below. b) Z-scores of the monthly velocity anomalies of crevassed areas compared to moulin-drained areas from 2015–2024 shown for three approximate elevation zones: lower-elevation 500–750m (blue), mid-elevation 750–950m (violet) and higher-elevation 950–1100m (magenta). Results within the cyan band (|Z|<2.58) show no significant velocity difference between crevasse areas and moulin-drained areas, at 99% confidence. Positive Z-scores indicate that velocity anomalies are higher in crevassed areas than moulin-drained areas; negative Z-scores indicate the opposite.

4.2 Seasonal variability in ice flow

We investigated whether there is a difference in ice flow speed between crevasse fields and moulin-drained areas over the melt season. Figure 13 shows the monthly area-composited velocity anomalies over the melt season averaged over 2015–2024. We also show the number of ITS_LIVE monthly velocity observations that passed our filtering criteria in Figure 14a. These numbers peak in the summer and become more sparse in the winter, when low solar illumination limits usable image acquisitions. The general ice flow direction is from the northeast to southwest. Figure 14a shows the monthly average velocity anomalies with 1σ error envelopes over the 2015–2024 study period. In moulin-drained areas, ice flow undergoes a strong seasonal cycle from May through September, which coincides with the melt season. These areas experience an average velocity anomaly of 30±68 m yr^{-1} in May, 57±95 m yr^{-1} in June, -12±63 m yr^{-1} in July, -3±60 m yr^{-1} in August and 2±41 m yr^{-1} in September. In crevasse fields, the seasonal pattern of ice flow is slightly different. Crevasse fields experience an average velocity anomaly of 27±56 m yr^{-1} in May, 55±90 m yr^{-1} in June, 4±66 m yr^{-1} in July, -2±56 m yr^{-1} in August and 0±41 m yr^{-1} in September. Both moulin-drained areas and crevasse fields experience the highest positive velocity anomalies in June, indicating a spatially pervasive spring-to-early-summer speedup for the entire region (Figure 13c). Ice flow slows significantly in July in moulin-drained areas, while in crevassed areas, ice velocity remains above average. In both moulin-drained and crevassed areas, ice velocity slows down to pre-summer velocities through August and September.

Results of the velocity anomaly Z-test between crevassed and moulin-drained areas across the three approximate elevation zones are shown in Figure 14b for all calendar months, averaged over 2015–2024. In May, the average velocity anomaly in crevassed areas at lower elevations was +36 m yr^{-1}; in moulin-drained areas in this same elevation range, the velocity anomaly was +48 m yr^{-1}. These are not significantly different (Z=-1.7, Fig 14b). In the mid-elevation range, the average velocity anomaly in crevassed areas was +15 m yr^{-1}, which was lower (Z=-2.5) than what we observed in moulin-drained areas, +28 m yr^{-1}. At the higher-elevation range, both areas have muted positive anomalies (+20 m yr^{-1} and +10 m yr^{-1} respectively) that are not significantly different (Z=1.9).

In June, both crevassed and moulin-drained areas at lower elevations continue to experience high (+46 m yr^{-1} and +48 m yr^{-1} respectively) velocity anomalies that are not significantly different (Z=-0.2). Crevassed and moulin-drained areas at mid-elevations experience high velocity anomalies (+57 m yr^{-1} and +52 m yr^{-1} respectively); these, too, are not significantly different (Z=0.6). At higher elevations, both crevassed and moulin-drained areas experience comparably higher velocity anomalies (+69 m yr^{-1} and +76 m yr^{-1} respectively; Z=-0.7).

In July, lower-elevation crevassed areas slow down (-19 m yr^{-1}) significantly less than moulin-drained areas (-42 m yr^{-1}, Z=4.8). At mid-elevations, crevassed areas experience nearly no change (-2 m yr^{-1}) while moulin-drained areas slow down (-12 m yr^{-1}); the difference is not significant (Z=2.4). At higher elevations, both crevassed and moulin-drained areas experience mildly positive anomalies on average (+26 m yr^{-1} and +31 m yr^{-1} respectively) that are not significantly different from one another (Z=-0.8).

In August, both areas at lower elevations continue to slow down similarly (-27 m yr^{-1} and -30 m yr^{-1} respectively; Z=0.6). The results are similar at mid-elevations (+4 m yr^{-1} and +15 m yr^{-1}

respectively; Z=-1.8). At higher elevations, the average velocity anomaly in crevassed areas was +26 m yr^{-1} which is significantly lower (Z=-2.6) than what we observed in moulin-drained areas +44 m yr^{-1}.

In September, both crevassed and moulin-drained areas across all three elevation zones slow down to pre-summer speeds, showing near-zero velocity anomalies overall that are statistically indistinguishable in crevasse fields and moulin-drained areas. This marks the end of the melt season. Crevasse fields and moulin-drained areas experience similar velocity anomalies over winter from September through March.

4.3 Time evolution of total crevassed area in Pakitsoq

We studied the time evolution in the total crevassed area of our study area in Pakitsoq. Figure 15 shows crevasse detections from the six MimiNet models described in Section 2.4. Figure 15a shows the total crevassed area observed each year over our ten-year study period (2015–2024), with error bars showing 1 sigma variations across the six models. There is no overall trend over the study period (R^2= 2.4 × 10^{-5}, p=0.989).

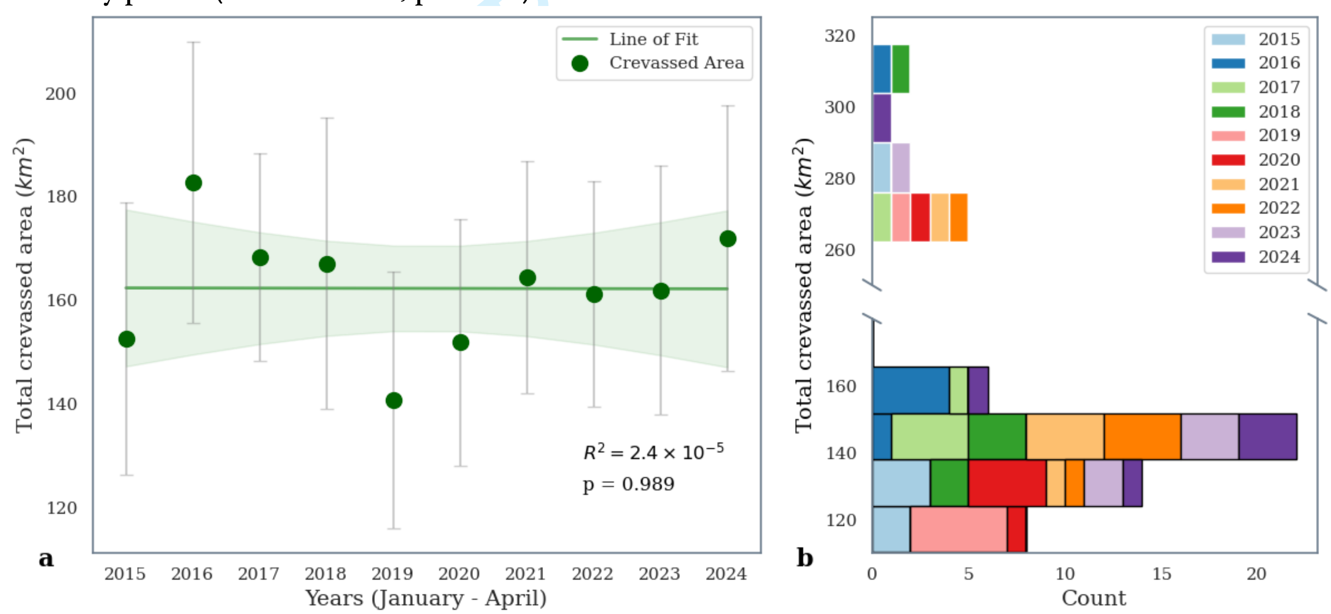

Figure 15: a) Time evolution of crevassed area in Pakitsoq, Greenland over 2015–2024 identified by six MimiNet models. Green circles show the total crevassed area over time, with gray error bars showing the 1 σ range across the results from the six models. Green line shows the least-squares fit to the time series, with shaded green area showing the 95% confidence interval. Values of R^2 and p are shown. b) Stacked histogram showing the total crevassed area over 2015–2024, colored by year, detected by the six models. Models trained on labels based on Sentinel-1 wintertime imagery are outlined in black, while models trained on labels based on WorldView summertime imagery are outlined in white.

In the first year of our study period, 2015, we found a total crevassed area of 153±26 km^2. The maximum total crevassed area over our 10-year study period was 183±27 km^2 in 2016. The minimum occurred in 2019; at 141±25 km^2 it is substantially lower than the area in other years but is still within measurement uncertainty of the study period mean, 162 km^2. We found that the overall standard deviation of the crevassed area was 12 km^2.

Figure 15b summarizes the total crevassed area from 2015–2024 calculated from the six models. The stacked bars outlined in black show the results from the five models trained on labels based on Sentinel-1 wintertime imagery, while those outlined in white show the results from the model trained on labels based on WorldView summertime imagery (Section 3.4). These results are significantly different from each other. The five models operating on wintertime imagery produce consistent results within 120–160 km^2, while the model operating on summertime imagery finds crevassed areas between 260–320 km^2 for all years. This variability may be the result of the difference in seasons (winter versus summer), image resolution, and acquisition sensors between the satellites. All models, whether using wintertime or summertime imagery, found that the highest crevassed area occurred in 2016 (orange, 13% above the mean) and the lowest crevassed area in 2019 (purple, 13% below the mean). This consistency between seasons gives further confidence in the accuracy of the model to identify crevasses on the ice surface and shows that there is detectable interannual variability in the size of crevasse fields.

5 Discussion

5.1 Persistence in crevasse field locations

As demonstrated in Figure 11k and Figure 12, MimiNet can identify the locations of crevasse fields from remote sensing imagery. With MimiNet, we were able to extend the crevasse fields identified by Hoffman and others (2018) who manually digitized crevasse fields from WorldView-1 optical imagery acquired in 2009 to 2011 with the 2015–2024 detections presented in this study. We find that the crevasse fields in Pakitsoq largely occupied the same locations across the two studies despite differences in the type of satellite imagery, detection methods, and the five-year time gap (2011–2015) inherent to the two datasets. Generally, crevasses open at the same locations on the ice sheet surface where steep bed topography causes high extensional strain rates (Echelmeyer and others, 1991; Cuffey and Paterson, 2010; Joughin and others, 2013). Both Hoffman and others (2018) and our results indicate this process. Slight differences in the locations of crevasse fields identified by Hoffman and others (2018) and by us could originate from image geolocation differences, crevasse detection methods, or from changes in crevasse field geometry. MimiNet detects a crevasse field based on the extent of the bright linear patch of crevasses on SAR imagery while Hoffman and others (2018) results show generally smaller crevasse fields, with boundaries differing by a few hundred meters. This difference stems from the limitation of manual delineation of crevasse fields on optical imagery where a crevasse may be obscured by snow cover. MimiNet, which uses SAR imagery, is not limited by the presence of snow and can therefore be applied to imagery collected at any time of year. The difference in the sizes of the crevasse fields is caused by the individual detection method and satellite imagery used; it does not occur as a change between 2009 and 2024.

5.2 Trends in Pakitsoq crevassed area

Our ten-year study of the total crevassed area across Pakitsoq, Greenland found interannual variability of ±13% with no overall trend over the full timeseries (Fig. 15a). This lack of a trend over the ten-year observation period contrasts with Colgan and others (2011), who found a significant increase in crevassed area of ~33 km^2 (5%) between 1985 and 2009 for a 608 km^2 region that overlaps with and extends south of our area. A linear increase in crevasse area between 1985 and 2009 would correspond to an average increase of 1.37 km^2 per year, or 0.2% of the study area per year. A significant advantage of our approach over this end-to-end comparison is the time series nature of our analysis, which yields a linear fit with uncertainties (Fig. 15a) and provides a range of possible changes in crevassed area over our 2015–2024 study period. The maximum rate of change allowed by the uncertainties on our fit is ±3.33 km^2 per year over our 629 km^2 study area, or +0.5% of the study area per year. This is consistent with the +0.2% per year found by Colgan and others (2011), although we emphasize that our finding was no trend. Similarly, their finding of a 5% increase in crevassed area between two study years is well within our detected interannual variability of 13%.

In central western Greenland, Chudley and others (2025) found a significant decrease in crevassed area (-14%) between the two years 2016 and 2021. They inferred that crevasse fields experienced active closure within their 5-year study period due to the slowdown of Sermeq Kujalleq which occurred in the latter half of the 2010s due to cooler oceanic temperatures (Khazender and others, 2019; Joughin and others, 2020). The local decrease in crevassed area observed by Chudley and others (2025) would likely also affect our nearby study area as well (Colgan and others, 2011). If we were to subset our crevassed area time series so that only 2016 and 2021 are compared, mirroring Chudley and others (2025), we would also find a significant decrease in crevassed area (-11%), comparable to their -14% findings. Conversely, our time series would yield a significant increase in crevassed area (+12%) if we only compared 2015 and 2024. Therefore, our full time series analysis is advantageous over previously published comparisons of individual years because we can identify the trend in crevassed area that accounts for interannual variability. Our findings in Pakitsoq suggest that the crevasse extent in nearby Sermeq Kujalleq may also exhibit interannual variability. This interannual variability could explain the pattern of varying expansion and reduction of crevassed area observed in specific years over a 36-year period found by Colgan and others (2011) and Chudley and others (2025), respectively.

5.3 Spatial variability of ice flow and inferences about the subglacial hydrologic system

We interpret the seasonal velocity patterns we observe in our study area in terms of the contrasting roles of moulins and crevasse fields in bringing meltwater to the ice-sheet bed. Moulins drain meltwater from large catchments that can exceed ~16 km^2 (Mejia and others, 2022) and deliver it to the bed at discrete locations. This delivery occurs quickly and relatively early in the melt season, allowing localized channels to form in the subglacial drainage system during June (Banwell and others, 2013; 2016) and persisting through at least August (Trunz and others, 2023). In contrast, moulins are almost entirely absent from all crevassed areas we identified (Figure 9), so the subglacial system there should lack the concentrated water influxes that drive the subglacial system to quickly channelize. If the closely spaced crevasses within a crevasse field do deliver water to the bed, each individual crevasse would have a much smaller catchment than a moulin, and would deliver only a small fraction of the meltwater volume compared to a moulin. We estimate that with average crevasse spacing of ~50 meters in Pakitsoq (Poinar, 2015) and length ~300 m (Figure 1b–c), the catchment size of each crevasse (~0.015 km^2) is one to three orders of magnitude smaller than that of a typical moulin (~0.2–16 km^2, Mejia and others, 2022). Therefore, a subglacial water flux through a single crevasse should be insufficient to develop a channelized drainage system under 700-meter-thick ice (Dow and others, 2014). Thus, if crevasses do deliver water to an inefficient drainage system at the bed, we would expect ice flow speeds to be relatively faster over the mid-to-late melt season because these meltwater inputs would increase pressures within the inefficient subglacial system. If crevasses do not convey meltwater to the bed, we would instead expect ice flow speeds within crevasse fields to be very similar to those in moulin-drained areas, following the ice-sheet coupling length of 3–8 ice thicknesses (Gudmundsson, 2003), which is ~5 km in our study area. We use our evidence to evaluate this general hypothesis.

We interpret the temporal variability in ice flow speed (Fig. 14) in terms of surface meltwater availability and the inferred evolution of the subglacial drainage system. The onset of the melt season in this region typically occurs from May to early June (Wang and others, 2007; Andrews and others, 2014; Mejia and others, 2021). Supraglacial lake drainage events in 2002–2018 in this area have been observed to occur as early as mid-May, where lake-draining moulins were activated, implying surface meltwater reaching the bed in moulin-drained areas (Morriss and others, 2013; Poinar and Andrews, 2021). This is consistent with our observations of higher May velocity anomalies in moulin-drained than in crevassed areas (Fig. 13, Fig. 14). From this, we infer that these newly activated moulins deliver meltwater to the bed, where it overwhelms and pressurizes the subglacial drainage system which is in its wintertime distributed state.

In June, the entire study area experiences substantial ice-flow speedup. In the moulin-drained portions of the study area, moulins develop by early June and begin to transport large amounts of meltwater to the distributed subglacial system (Morris and others, 2013; Fitzpatrick and others, 2014; Williamson and others, 2018; Andrews and others, 2018; Poinar and Andrews, 2021; Mejia and others, 2022). This temporarily increases subglacial water pressure, but the subglacial hydrologic system quickly adapts to this point-source meltwater delivery by transitioning into an efficient channelized system by mid to late June (Bartholomew and others, 2010), limiting ice acceleration for the rest of the melt season (Andrews and others, 2018). We see evidence of this in Figure 14a over July through September. In crevassed areas, the velocity anomaly data implies that crevasses also begin to transport meltwater to the bed in June, but that the subglacial hydrologic system remains in a distributed state.

In July, the velocity data show slowing ice flow speeds when compared to June (Fig. 13, 14) indicating that meltwater across the moulin-drained areas continues to reach a channelized subglacial system (Koziol and Arnold, 2018). Crevassed areas also continue to deliver meltwater to the bed; however, the water volume flux through the thousands of individual crevasses in our study area is inadequate to form subglacial channels, leaving the subglacial system in a distributed state. Moulin-drained areas above 950 m a.s.l. likely drain water to a weakly connected subglacial drainage system (Andrews and others, 2014), explaining similar flow-speed variability as crevassed areas in higher-elevation regions (Fig. 14b). High ice-overburden pressure at these inland locations likely shrinks the subglacial channels over a timescale of hours to days (Nye, 1953; Catania and Neumann, 2010), and the low subglacial water pressure gradient prohibits the faster water motion that would be needed to re-expand the channels (Dow and others, 2014). These factors limit the efficiency of the subglacial drainage system at inland locations.

We infer that the subglacial drainage system underneath moulin-drained areas below 750 m a.s.l. remains channelized through August, allowing ice flow speeds to continue to decline from their June peak (Figure 13a, 14a). However, in moulin-drained areas above 750 m a.s.l., this pattern is absent. We interpret this as evidence of a fewer number of moulins and a less pervasive subglacial channelization there. We infer that in July, decreasing surface melt rates cause the subglacial channels to begin shrinking. Therefore, while moulins in moulin-drained areas continue to deliver meltwater to the bed through August, the reduced volume of the channelized drainage system allows ice flow speeds to rise, while still remaining slower than peak summer (Fig. 13a, c, comparing August to June). Due to decreasing surface melt rates, crevassed areas receive less meltwater flux compared to peak melt in June and July, and the subglacial system remains in a distributed state, allowing stable ice flow rates in crevassed areas.

In September, surface melt rates drop as the end of the melt season approaches. With insufficient melt inputs to maintain channels, the subglacial system underneath the entire study area returns to a distributed state. Our velocity anomaly observations indicate that this transition to its pre-summer state is complete by October (Fig. 14).

5.4 Comparison to other crevasse detection methods

While MimiNet does not detect individual crevasses, it is unique in that it can detect crevasse fields, along with supraglacial lakes and remnant streams from winter and early spring Sentinel-1 SAR imagery. Recent automated crevasse detection studies have been able to locate individual crevasses on Antarctic ice shelves (Lai and others, 2020; Zhao and others, 2022; Surawy-Stepney and others, 2023). The key difference is the size of the crevasses being observed. Individual crevasses on ice shelves can be hundreds of meters to multiple kilometers wide, making their individual detection in imagery feasible, even in low or moderate resolution imagery such as MODIS-based mosaics for Antarctica at 250-meter resolution (Lai and others, 2020). The kilometer-scale size of a single crevasse on Antarctic ice shelves is comparable to the broad-scale output of MimiNet for Greenland: crevasse fields with dimensions of ~1–5 kilometers. These size differentials makes single-crevasse detection on the ablation zone in Greenland infeasible on moderate resolution imagery.

MimiNet complements existing DEM-based crevasse detection methods that have been optimized for the Greenland Ice Sheet margin (Chudley and others, 2025). The method employed by Chudley and others (2025) uses DEMs produced from high-resolution optical imagery to detect individual crevasses with a minimum width and depth of 10 meters. MimiNet detects crevasse fields composed of crevasses with a minimum width that we estimate at half of a Sentinel-1 SAR image pixel, or ~5 meters. Due to being trained with SAR imagery, MimiNet is not limited by daylight or cloud conditions and has new image acquisitions regularly; optical-imagery-based DEMs do not have these advantages. The DEM-based method excels at detecting individual, large crevasses, which are most often found on fast-flowing outlet glaciers or near ice sheet margins. MimiNet complements this with its ability to detect crevasse fields composed of narrower crevasses, which are typically found farther inland. Indeed, the crevasse detections in the Pakitsoq area by Chudley and others (2025) are primarily below 900 m a.s.l., whereas MimiNet finds crevasse fields that extend ~15 km farther inland, reaching the upper limit of our study area at 1100 m a.s.l. Chudley and others (2025) find isolated crevasses at 900–1100 m a.s.l., however we find that many of those detections are better aligned with MimiNet detected streams than with crevasse fields. This is consistent with the rough sizes of these features: higher-elevation crevasses are likely to be narrow (5–10 m), whereas streams can range from 1–30 m wide in this region (Yang and others, 2013). This suggests the DEM method by Chudley and others (2025) may be detecting eroded supraglacial stream channels, not crevasses, above 900 m a.s.l. With weather-independent high resolution SAR imagery, MimiNet makes it possible to locate crevasse fields throughout the ablation zone.

6 Conclusion

We provide the first deep-learning CNN-based automated crevasse detection from Sentinel-1 SAR imagery suitable for Greenland: MimiNet, a Tensorflow-based CNN model that runs on Ghub. In applying the MimiNet workflow to study the interannual variability in the locations and size of the crevassed areas in Pakitsoq, central western Greenland. We found no overall trend in the crevasse extent over 2015–2024 contrasting the increasing trend in crevassed area previously identified in the region (Chudley and others, 2025). The size and locations of crevasse fields were highly persistent over our 10-year study period, in agreement with a previous work (Hoffman and others, 2018). Throughout our study period, we identified clear seasonal velocity signals with a spring speedup in June and slowdown which occurred through August and September of each year. By using flow speed anomalies as a window onto the efficiency of the subglacial drainage network, we infer that crevasse fields in Pakitsoq deliver meltwater to the bed but while moulin-drained areas are better able to efficiently route meltwater directly to the bed and drive seasonal changes in the subglacial drainage system structure and efficiency. Our workflow enables future research to study the spatial distribution and temporal trends in crevasse fields on ice masses surveyed by the Sentinel-1 satellite constellation. We envision that the improvement of SAR-despeckling techniques will lead to highly accurate crevasse detection results.

Supplementary Material

The supplementary material for this article can be found at [url].

Code and data availability

The workflow for crevasse field detection in Pakitsoq, Greenland is available on Zenodo (https://doi.org/10.5281/zenodo.15116011) as well as accessible as a Ghub Tool (https://theghub.org/resources/crevassedetect).

Author Contributions

KP, NK and SN conceived the study. NK and KP curated the data. NK, KP, and MV conducted the data analysis. KP, JB, and SN acquired the funding. NK and MV performed data collection. NK, KP, SN, JB, and JM designed the methods. KP, SN, and JB managed and coordinated the study. KP, SN, and JB provided the computing resources. NK, KP, and JM designed and implemented the code. KP, SN, JB, and JM provided supervision. NK and KP validated the research outputs. NK and KP prepared the data presentation. NK and KP prepared the original manuscript. All authors contributed to reviewing and editing the final manuscript.

Acknowledgements

This work was supported by NASA award 80NSSC19K0054 (KP) and NSF award 2004302 (JB, SN, and KP). Computing resources for this work were supplied and supported by the University at Buffalo's Center for Computational Research (CCR).

Competing Interests

The authors declare no competing interests.

References

Abadi M and 21 others (2016) {TensorFlow}: a system for {Large-Scale} machine learning. In *12th USENIX symposium on operating systems design and implementation (OSDI 16)* (pp. 265-283).

Akeret J, Chang C, Lucchi A and Refregier A (2016) Radio frequency interference mitigation using deep convolutional neural networks. Retrieved from https://arxiv.org/abs/1609.09077

Alley RB, Dupont TK, Parizek BR and Anandakrishnan S (2005) Access of surface meltwater to beds of sub-freezing glaciers: preliminary insights. *Annals of Glaciology*, *40*, 8-14. https://doi.org/10.3189/172756405781813483

Alzubaidi L and 9 others (2021) Review of deep learning: concepts, CNN architectures, challenges, applications, future directions. *Journal of Big Data*, *8*, pp.1-74. https://doi.org/10.1186/s40537-021-00444-8

Andrews LC and 7 others (2014) Direct observations of evolving subglacial drainage beneath the Greenland Ice Sheet. *Nature*, *514*(7520), 80-83. https://doi.org/10.1038/nature13796

Andrews LC and 8 others (2018) Seasonal evolution of the subglacial hydrologic system modified by supraglacial lake drainage in western Greenland. *Journal of Geophysical Research: Earth Surface*, *123*(6), 1479-1496. https://doi.org/10.1029/2017JF004585

Banwell AF, Willis IC, and Arnold NS (2013) Modeling subglacial water routing at Paakitsoq, W Greenland. *Journal of Geophysical Research: Earth Surface*, *118*(3), 1282–1295. https://doi.org/10.1002/jgrf.20093

Banwell A, Hewitt I, Willis I, and Arnold N (2016) Moulin density controls drainage development beneath the Greenland ice sheet. *Journal of Geophysical Research: Earth Surface*, *121*(12), 2248-2269. https://doi.org/10.1002/2015JF003801

Bartholomew I, Nienow P, Mair D, Hubbard A, King MA and Sole A (2010). Seasonal evolution of subglacial drainage and acceleration in a Greenland outlet glacier. *Nature Geoscience*, *3*(6), 408-411. https://doi.org/10.1038/ngeo863

Baumhoer CA, Dietz AJ, Kneisel C and Kuenzer C (2019) Automated Extraction of Antarctic Glacier and Ice Shelf Fronts from Sentinel-1 Imagery Using Deep Learning. *Remote Sensing*, *11*(21), 2529. https://doi.org/10.3390/rs11212529

Buduma N, Buduma N and Papa J (2022) *Fundamentals of deep learning*. "O'Reilly Media, Inc.".

Catania GA and Neumann TA (2010) Persistent englacial drainage features in the Greenland Ice Sheet. *Geophysical Research Letters*, *37*(2). https://doi.org/10.1029/2009GL041108

Cheng D and 6 others (2021) Calving Front Machine (CALFIN): glacial termini dataset and automated deep learning extraction method for Greenland, 1972–2019. *The Cryosphere*, *15*(3), 1663–1675. https://doi.org/10.5194/tc-15-1663-2021

Chu X, Yao X, Duan H, Chen C, Li J and Pang W (2022) Glacier extraction based on high-spatial-resolution remote-sensing images using a deep-learning approach with attention mechanism. *The Cryosphere*, *16*(10), 4273-4289. https://doi.org/10.5194/tc-16-4273-2022

Chudley TR and 7 others (2021) Controls on Water Storage and Drainage in Crevasses on the

Greenland Ice Sheet. *Journal of Geophysical Research: Earth Surface*, *126*(9). https://doi.org/10.1029/2021jf006287

Chudley TR, Howat I, King M and MacKie EJ (2025) Increased crevassing across accelerating Greenland Ice Sheet margins. *Nature Geoscience*, 1-6. https://doi.org/10.1038/s41561-024-01636-6

Clark S (2023) Jupyter Lab (202210). Retrieved from https://theghub.org/resources/jupyterlab70

Colgan W and 7 others (2011) An increase in crevasse extent, West Greenland: Hydrologic implications. *Geophysical Research Letters*, *38*(18), n/a-n/a. https://doi.org/10.1029/2011gl048491

Colgan W and 6 others (2016) Glacier crevasses: Observations, models, and mass balance implications. *Reviews of Geophysics*, *54*(1), 119–161. https://doi.org/10.1002/2015rg000504

Cook JC (1956) Some observations in a northwest Greenland crevasse, *Eos Trans. AGU*, 37(6), 715–718, https://doi.org/10.1029/TR037i006p00715.

Cuffey KM and Paterson WSB (2010) *The physics of glaciers*. Academic Press.

Das SB and 6 others (2008) Fracture Propagation to the Base of the Greenland Ice Sheet During Supraglacial Lake Drainage. *Science*, *320*(5877), 778–781. https://doi.org/10.1126/science.1153360

Dow CF, Kulessa B, Rutt IC, Doyle SH and Hubbard A (2014) Upper bounds on subglacial channel development for interior regions of the Greenland ice sheet. *Journal of Glaciology*, *60*(224), 1044-1052. https://doi.org/10.3189/2014JoG14J093

Echelmeyer K, Clarke TS and Harrison WD (1991) Surficial glaciology of Jakobshavns Isbræ, West Greenland: Part I. Surface morphology. *Journal of Glaciology*, *37*(127), 368-382. https://doi.org/10.3189/S0022143000005803

Eder K, Reidler C, Mayer C and Leopold M (2008) Crevasse detection in Alpine areas using ground penetrating radar as a component for a mountain guide system. *The International Archives of the Photogrammetry, Remote Sensing and Spatial Information Sciences*, *37*, 837-841.

European Space Agency (2014) *Sentinel-1 User Handbook*, GMES-S1OP-EOPG-TN-13-0001, ESRIN, Frascati, Italy. https://sentinel.esa.int

Fitzpatrick AAW and 9 others (2014) A decade (2002–2012) of supraglacial lake volume estimates across Russell Glacier, West Greenland. *The Cryosphere*, *8*(1), 107-121. https://doi.org/10.5194/tc-8-107-2014

Flowers GE (2010) Glacier hydromechanics: early insights and the lasting legacy of three works by Iken and colleagues. *Journal of Glaciology*, *56*(200), 1069-1078. https://doi.org/10.3189/002214311796406103

Gardner AS and 8 others (2025) ITS_LIVE global glacier velocity data in near real time. *EGUsphere*, *2025*, 1-29. https://doi.org/10.5194/egusphere-2025-392

Gorelick N, Hancher M, Dixon M, Ilyushchenko S, Thau D and Moore R (2017) Google Earth Engine: Planetary-scale geospatial analysis for everyone. *Remote Sensing of Environment*, *202*, 18–27. https://doi.org/10.1016/j.rse.2017.06.031

Gu J and 10 others (2018) Recent advances in convolutional neural networks. *Pattern recognition*, *77*, pp.354-377. https://doi.org/10.1016/j.patcog.2017.10.013

Gudmundsson GH (2003) Transmission of basal variability to a glacier surface. *Journal of Geophysical Research: Solid Earth*, *108*(B5). https://doi.org/10.1029/2002JB002107

Gulley JD, Grabiec M, Martin JB, Jania J, Catania GA and Glowacki PS (2012) The effect of discrete recharge by moulins and heterogeneity in flow-path efficiency at glacier beds on subglacial hydrology. Journal of Glaciology, 58(211), 926–940. https://doi.org/10.3189/2012JoG11J189

Herrmann O and 6 others (2023) Out-of-the-box calving front detection method using deep-learning. *The Cryosphere Discussions*, *2023*, 1-24. https://doi.org/10.5194/tc-17-4957-2023

Herzfeld UC, Trantow T, Lawson M, Hans J and Medley G (2021) Surface heights and crevasse morphologies of surging and fast-moving glaciers from ICESat-2 laser altimeter data-Application of the density-dimension algorithm (DDA-ice) and evaluation using airborne altimeter and Planet SkySat data. *Science of Remote Sensing*, *3*, 100013. https://doi.org/10.1016/j.srs.2020.100013

Hoffman MJ and 7 others (2018) Widespread Moulin Formation During Supraglacial Lake Drainages in Greenland. *Geophysical Research Letters*, *45*(2), 778–788. https://doi.org/10.1002/2017gl075659

Hooke RL (1989) Englacial and subglacial hydrology: a qualitative review. *Arctic and Alpine Research*, *21*(3), 221-233. https://doi.org/10.1080/00040851.1989.12002734

Howat IM, Negrete A and Smith BE (2014) The Greenland Ice Mapping Project (GIMP) land classification and surface elevation datasets. *The Cryosphere*, *8*, 1509-1518. https://doi.org/10.5194/tc-8-1509-2014

Joughin I and 9 others (2013) Influence of ice-sheet geometry and supraglacial lakes on seasonal ice-flow variability. *The Cryosphere*, *7*(4), 1185-1192. https://doi.org/10.5194/tc-7-1185-2013

Joughin I, Shean DE, Smith BE and Floricioiu D (2020) A decade of variability on Jakobshavn Isbræ: ocean temperatures pace speed through influence on mélange rigidity. *The Cryosphere*, *14*(1), 211-227.

Kaluzienski L, Koons P, Enderlin E, Hamilton G, Courville Z and Arcone S (2019) Crevasse initiation and history within the McMurdo Shear Zone, Antarctica. *Journal of Glaciology*, *65*(254), 989-999. https://doi.org/10.1017/jog.2019.65

Khazendar A and 13 others (2019) Interruption of two decades of Jakobshavn Isbrae acceleration and thinning as regional ocean cools. *Nature Geoscience*, *12*(4), 277-283. https://doi.org/10.1038/s41561-019-0329-3

Koike K, Yoshida H, Omura M, Shibuya K and Doi K (2012) Temporal changes in crevasses in the middle Slessor Glacier, Coats Land, East Antarctica through SAR data analysis. *Earth, planets and space*, *64*, 257-267. https://doi.org/10.5047/eps.2011.10.003

Koziol C, Arnold N, Pope A and Colgan W (2017) Quantifying supraglacial meltwater pathways in the Paakitsoq region, West Greenland. *Journal of Glaciology*, *63*(239), 464–476. https://doi.org/10.1017/jog.2017.5

Koziol CP and Arnold N (2018) Modelling seasonal meltwater forcing of the velocity of land-terminating margins of the Greenland Ice Sheet. *The Cryosphere*, *12*(3), 971-991. https://doi.org/10.5194/tc-12-971-2018

Krawczynski MJ, Behn MD, Das SB and Joughin I (2009) Constraints on the lake volume required for hydro-fracture through ice sheets. *Geophysical Research Letters*, *36*(10). https://doi.org/10.1029/2008GL036765

Lai C-Y and 7 others (2020) Vulnerability of Antarctica's ice shelves to meltwater-driven fracture. *Nature*, *584*(7822), 574–578. https://doi.org/10.1038/s41586-020-2627-8

LeCun Y, Bengio Y and Hinton G (2015) Deep learning. *Nature*, *521*(7553), 436-444. https://doi.org/10.1038/nature14539

Libert L, Wuite J and Nagler T (2022) Automatic delineation of cracks with Sentinel-1 interferometry for monitoring ice shelf damage and calving. *The Cryosphere*, *16*(4), 1523-1542. https://doi.org/10.5194/tc-16-1523-2022

Loebel E and 7 others (2023) Calving front monitoring at sub-seasonal resolution: a deep learning application to Greenland glaciers. *The Cryosphere Discussions*, *2023*, 1-21. https://doi.org/10.5194/tc-18-3315-2024

Long J, Shelhamer E and Darrell T (2015) Fully convolutional networks for semantic segmentation. In *Proceedings of the IEEE conference on computer vision and pattern recognition* (pp. 3431-3440).

Lüthi MP and 7 others (2015) Heat sources within the Greenland Ice Sheet: dissipation, temperate paleo-firn and cryo-hydrologic warming. *The Cryosphere*, *9*(1), 245-253. https://doi.org/10.5194/tc-9-245-2015

Marin C and 8 others (2020) Use of Sentinel-1 radar observations to evaluate snowmelt dynamics in alpine regions. *The Cryosphere*, *14*(3), 935-956. https://doi.org/10.5194/tc-14-935-2020

Marsh OJ, Price D, Courville ZR and Floricioiu D (2021) Crevasse and rift detection in Antarctica from TerraSAR-X satellite imagery. *Cold Regions Science and Technology*, *187*(103284). https://doi.org/10.1016/j.coldregions.2021.103284

Marshall E, Henderson S and Cherian D (2022) e-marshall/itslive: itslive tutorial updates (v.1.0.0). Zenodo. https://doi.org/10.5281/zenodo.6804325

McGrath D, Colgan W, Steffen K, Lauffenburger P, and Balog J (2011) Assessing the summer water budget of a moulin basin in the Sermeq Avannarleq ablation region, Greenland ice sheet. Journal of Glaciology, 57(205), 954-964. https://doi.org/10.3189/002214311798043735

Mejia JZ and 6 others (2021) Isolated cavities dominate Greenland Ice Sheet dynamic response to lake drainage. *Geophysical Research Letters*, *48*(19), e2021GL094762. https://doi.org/10.1029/2021GL094762

Mejia JZ and 7 others (2022) Moulin density controls the timing of peak pressurization within the Greenland Ice Sheet's subglacial drainage system. *Geophysical Research Letters*, *49*(22), e2022GL100058. https://doi.org/10.1029/2022GL100058

Mohajerani Y, Wood M, Velicogna I and Rignot E (2019) Detection of Glacier Calving Margins with Convolutional Neural Networks: A Case Study. *Remote Sensing*, *11*(1), 74. https://doi.org/10.3390/rs11010074

Moolayil J and Moolayil J (2019) Keras in action. *Learn Keras for Deep Neural Networks: A Fast-Track Approach to Modern Deep Learning with Python*, 17-52. https://doi.org/10.1007/978-1-4842-4240-7_2

Morlighem M and others (2022) IceBridge BedMachine Greenland (IDBMG4, Version 5) [Data Set] Boulder, Colorado USA. NASA National Snow and Ice Data Center Distributed Active Archive Center. https://doi.org/10.5067/GMEVBWFLWA7X. Date Accessed 03-11-2025.

Morriss BF and 7 others (2013) A ten-year record of supraglacial lake evolution and rapid drainage in West Greenland using an automated processing algorithm for multispectral imagery. *The Cryosphere*, *7*(6), 1869-1877. https://doi.org/10.5194/tc-7-1869-2013

Mouginot J and 8 others (2019) Forty-six years of Greenland Ice Sheet mass balance from 1972 to

2018. *Proceedings of the National Academy of Sciences*, *116*(19), 9239–9244. https://doi.org/10.1073/pnas.1904242116

Nienow PW, Sole AJ, Slater DA and Cowton TR (2017). Recent advances in our understanding of the role of meltwater in the Greenland Ice Sheet system. *Current Climate Change Reports*, *3*, 330-344. https://doi.org/10.1007/s40641-017-0083-9

Nye JF (1955) Comments on Dr. Loewe's letter and notes on crevasses. *Journal of Glaciology*, *2*(17), 512-514. https://doi.org/10.3189/S0022143000032652

Pedregosa F and 15 others (2011) Scikit-learn: Machine learning in Python. *the Journal of machine Learning research*, *12*, 2825-2830.

Phillips T, Rajaram H, Colgan W, Steffen K and Abdalati W (2013) Evaluation of cryo-hydrologic warming as an explanation for increased ice velocities in the wet snow zone, Sermeq Avannarleq, West Greenland. *Journal of Geophysical Research: Earth Surface*, *118*(3), 1241-1256. https://doi.org/10.1002/jgrf.20079

Pings CJ (1961) Temperature distribution near a crevasse. *Journal of Glaciology*, *3*(30), 985-996. https://doi.org/10.3189/S0022143000017391

Poinar K (2015) *The influence of meltwater on the thermal structure and flow of the Greenland Ice Sheet* (Doctoral dissertation)

Poinar K and Andrews LC (2020) Challenges in predicting Greenland supraglacial lake drainages at the regional scale. *The Cryosphere Discussions*, *2020*, 1-46. https://doi.org/10.5194/tc-15-1455-2021

Poinar K, Joughin I, Lenaerts JT and Van Den Broeke MR (2016) Englacial latent-heat transfer has limited influence on seaward ice flux in western Greenland. *Journal of Glaciology*, *63*(237), 1-16. https://doi.org/10.1017/jog.2016.103

Poinar K, Joughin I, Lilien D, Brucker L, Kehrl L and Nowicki S (2017) Drainage of Southeast Greenland firn aquifer water through crevasses to the bed. *Frontiers in Earth Science*, *5*, 5. https://doi.org/10.3389/feart.2017.00005

Ravanel L, Lacroix E, Le Meur E, Batoux P and Malet E (2022) Multiparameter monitoring of crevasses on an Alpine glacier to understand formation and evolution of snow bridges. *Cold Regions Science and Technology*, *203*, 103643. https://doi.org/10.1016/j.coldregions.2022.103643

Rignot E, Echelmeyer K and Krabill W (2001) Penetration depth of interferometric synthetic-aperture radar signals in snow and ice. *Geophysical Research Letters*, *28*(18), 3501-3504. https://doi.org/10.1029/2000GL012484

Ronneberger O, Fischer P and Brox T (2015) U-Net: Convolutional Networks for Biomedical Image Segmentation. Retrieved from https://arxiv.org/abs/1505.04597

Schoof C (2010) Ice-sheet acceleration driven by melt supply variability. *Nature*, *468*(7325), 803–806. https://doi.org/10.1038/nature09618

Smith LC and 15 others (2015) Efficient meltwater drainage through supraglacial streams and rivers on the southwest Greenland ice sheet. *Proceedings of the National Academy of Sciences*, *112*(4), 1001-1006. https://doi.org/10.1073/pnas.1413024112

Sperhac JM and 9 others (2021). GHub: Building a glaciology gateway to unify a community. *Concurrency and Computation: Practice and Experience*, *33*(19), p.e6130. https://doi.org/10.1002/cpe.6130

Surawy-Stepney T, Hogg AE, Cornford SL and Hogg DC (2023) *Mapping Antarctic Crevasses and their Evolution with Deep Learning Applied to Satellite Radar Imagery*. Copernicus GmbH. Retrieved from http://dx.doi.org/10.5194/tc-2023-42

Surdu CM, Duguay CR, Brown LC and Fernández Prieto D (2014) Response of ice cover on shallow lakes of the North Slope of Alaska to contemporary climate conditions (1950–2011): radar remote-sensing and numerical modeling data analysis. *The Cryosphere*, *8*(1), 167-180. https://doi.org/10.5194/tc-8-167-2014

Taurisano A, Tronstad S, Brandt O and Kohler J (2006) On the use of ground penetrating radar for detecting and reducing crevasse-hazard in Dronning Maud Land, Antarctica. *Cold Regions Science and Technology*, *45*(3), 166-177. https://doi.org/10.1016/j.coldregions.2006.03.005

TensorFlow Developers (2023) TensorFlow (v2.15.0). Zenodo. https://doi.org/10.5281/zenodo.10126399

Terven J, Cordova-Esparza DM, Ramirez-Pedraza A, Chavez-Urbiola EA and Romero-Gonzalez JA (2024) Loss functions and Metrics in Deep Learning. *arXiv preprint arXiv:2307.02694*. https://doi.org/10.48550/arXiv.2307.02694

Thomsen HH, Olesen OB, Braithwaite RJ and Weidick A (1989) Greenland ice-margin programme, a pilot study at Pâkitsoq, north-east of Jakobshavn, central West Greenland. *Rapport Grønlands Geologiske Undersøgelse*, *145*, 50-53. https://doi.org/10.34194/rapggu.v145.8073

Thompson SS, Cook S, Kulessa B, Winberry JP, Fraser AD and Galton-Fenzi BK (2020) Comparing satellite and helicopter-based methods for observing crevasses, application in East Antarctica. *Cold Regions Science and Technology*, *178*, 103128.

Trunz C and 6 others (2023) Observed and modeled moulin heads in the Pâkitsoq region of

Greenland suggest subglacial channel network effects. *The Cryosphere*, *17*(12), 5075-5094. https://doi.org/10.5194/tc-17-5075-2023

van den Broeke and 7 others (2016) On the recent contribution of the Greenland ice sheet to sea level change. *The Cryosphere*, *10*(5), 1933–1946. https://doi.org/10.5194/tc-10-1933-2016

van de Wal RSW and 10 others (2015) Self-regulation of ice flow varies across the ablation area in south-west Greenland. *The Cryosphere*, *9*(2), 603-611. https://doi.org/10.5194/tc-9-603-2015

Veci L, Lu J, Foumelis M and Engdahl M (2017) ESA's multi-mission Sentinel-1 toolbox. In *EGU General Assembly Conference Abstracts* (p. 19398).

Walker B and Ray L (2019) Multi-class crevasse detection using ground penetrating radar and feature-based machine learning. In *IGARSS 2019-2019 IEEE International Geoscience and Remote Sensing Symposium* (pp. 3578-3581). IEEE. https://doi.org/10.1109/IGARSS.2019.8899148

Wang L, Sharp M, Rivard B and Steffen K (2007) Melt season duration and ice layer formation on the Greenland ice sheet, 2000–2004. *Journal of Geophysical Research: Earth Surface*, *112*(F4). https://doi.org/10.1029/2007JF000760

Williamson AG, Banwell AF, Willis IC and Arnold NS (2018) Dual-satellite (Sentinel-2 and Landsat 8) remote sensing of supraglacial lakes in Greenland. *The Cryosphere*, *12*(9), 3045-3065. https://doi.org/10.5194/tc-12-3045-2018

Yang K and Smith LC (2013) Supraglacial streams on the Greenland Ice Sheet delineated from combined spectral–shape information in high-resolution satellite imagery. *IEEE Geoscience and Remote Sensing Letters*, *10*(4), 801-805. https://doi.org/10.1109/LGRS.2012.2224316

Zeiler MD and Fergus R (2014) Visualizing and understanding convolutional networks. In *Computer Vision–ECCV 2014: 13th European Conference, Zurich, Switzerland, September 6-12, 2014, Proceedings, Part I 13* (pp. 818-833). Springer International Publishing. https://doi.org/10.1007/978-3-319-10590-1_53

Zhang E, Liu L, Huang L and Ng KS (2021) An automated, generalized, deep-learning-based method for delineating the calving fronts of Greenland glaciers from multi-sensor remote sensing imagery. *Remote Sensing of Environment*, *254*, 112265. https://doi.org/10.1016/j.rse.2020.112265

Zhao J, Liang S, Li X, Duan Y and Liang L (2022) Detection of Surface Crevasses over Antarctic Ice Shelves Using SAR Imagery and Deep Learning Method. *Remote Sensing*, *14*(3), 487. https://doi.org/10.3390/rs14030487

Supplementary Material

Supplementary Material for Crevasse locations and meltwater delivery to the bed in Pakitsoq, Greenland: Results from MimiNet, a new deep-learning model for crevasse detection

Naureen Khan[1], Kristin Poinar[1,2], Jason Briner[1], Sophie Nowicki[1,2], Jessica Mejia[1,3] and Mary Verné[1]

University at Buffalo, NY, Department of Earth Sciences[1], RENEW Institute[2], Syracuse University, NY, Department of Earth and Environmental Sciences[3]

Journal of Glaciology

Supplementary Material

S1. Sensitivity testing on input datasets

We tested and evaluated the sensitivity of our model to different versions of input datasets of Sentinel-1 SAR imagery over our training region. We tested the performance of the HH single co-polarization mode and the HV dual-band cross-polarization mode input datasets in our model. For both modes, we generated the median image across all acquisition dates in January 2020 (the median of 17 scenes) and also tested single-scene image acquisitions from Jan 13, 2020. The key difference between a single-date image and a median image is that the median image removes the majority of the speckle noise generated from SAR backscatter, facilitating feature detection. We trained our model on these four variations of input datasets to find the optimal input dataset that yielded the highest prediction accuracy, the lowest prediction loss, and a high IoU for the crevasse field class. Figure 7 shows the training labels for region D used for the input sensitivity testing followed by the four input variations of HH and HV polarization of the single January 13 scene and the median January image. As Figure 7 shows, both single-date images from HH and HV polarization contain a large amount of speckle noise. The median image from HH polarization appears relatively speckle-free and the majority of crevasse fields and supraglacial streams are distinctively bright and correspond well with input labels. The median image from HV polarization appears speckle-free, but crevasse fields and supraglacial streams are slightly darker. We trained models on four different permutations of polarization (HV and HH) and scene selection (median and single-scene images). We trained all models for 700 epochs. Figure S1b-e shows our model sensitivity results overlayed on the four input dataset variations.

The model trained on the HH polarization of the January 13, 2020 single-scene image produced predictions yielding 80% accuracy, 46% loss, 66% mean IoU and 35% crevasse IoU (Fig. S1). The model trained on HV polarization of the January 13, 2020 single-scene image produced predictions yielding 82% accuracy, 44% loss, 70% mean IoU and 48% crevasse IoU, a slightly better performance overall than the single-scene HH image. Both of these models trained on the noisy single-scene images are capable of picking up the outlines of crevasse fields; however, the detections are less precise within the crevasse fields. Both models detected only a small percentage of the labeled supraglacial streams. The model trained on the median image of HH polarization produced better results: 94% accuracy, 16% loss, 83% mean IoU and 73% crevasse field IoU. The model trained on HV polarization of January 2020 median images produced predictions yielding 83% accuracy, 42% loss, 71% mean IoU and 54% crevasse field IoU, a slightly worse performance overall than the median HH image. With both median-based inputs, the model identifies crevasse fields well. However, the model trained on HV-polarized median images does not detect any supraglacial streams and the model trained on a HV-polarized single scene erroneously classifies the bright speckle noise as supraglacial streams. We find the HH-polarized median images yield the highest evaluation metrics and most accurate predictions of both crevasse fields and supraglacial streams/lakes, and therefore use the HH-polarized median image dataset to train our model.

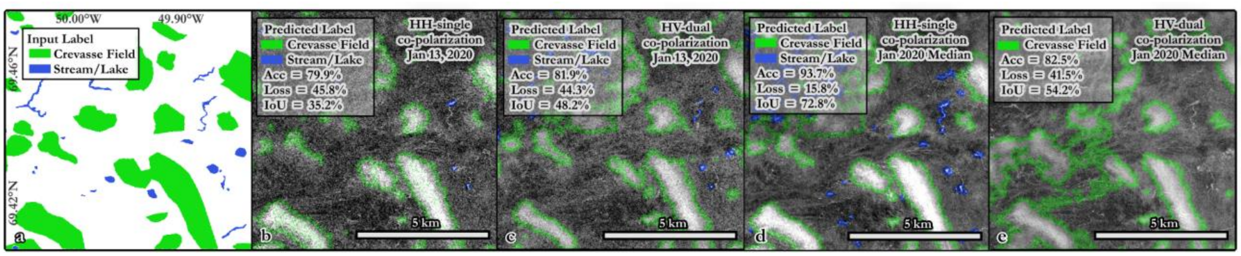

Figure S1: Sensitivity testing on input datasets for study region D: a) Labels of crevasse fields and supraglacial streams/lakes. b) Sentinel-1 HH single co-polarization scene acquired January 13, 2020. c) HV dual band cross-polarization scene acquired January 13, 2020. d) HH single co-polarization and e) HV dual co-polarization of the pixel-by-pixel median of 17 scenes acquired over January 2020. Training predictions are overlain on the images in panels b-e with metric scores (accuracy, loss and IoU) shown. The IoU score shown is for crevasse fields only, not the mean IOU across all classes.

S2. Sensitivity testing on model hyperparameters

In Table S1, we present parameters and results from model runs where we tested performance across multiple hyperparameter values. The hyperparameters we tested were the number of epochs, the learning rate, the optimizer function, and the dropout rate, as we found that these significantly affected model performance. We also explored tuning filter sizes, batch sizes, and the type of kernel initializer, but we found much less response in model performance across these, so they are not included in Table S1. All model runs shown used the pixel-by-pixel median of the Sentinel-1 HH single co-polarization scenes acquired over January 2020 as the training input dataset. For the optimizer functions, we show results with the Adaptive Moment Estimation (Adam) optimizer, the Stochastic Gradient Descent (SGD) optimizer and the Root Mean Square Propagation (RMSProp) optimizer. We used manual data augmentation, achieved by rotating all training images and their associated labels 90 degrees clockwise to increase the dataset size, and found that it substantially improved model performance. We evaluated the model performance using the metrics IoU, accuracy, and loss evaluated at the end of the model run.

*Table S1: Model hyperparameter tuning across the number of epochs, learning rate values, type of optimizer function (Adam, Stochastic Gradient Descent and RMSprop), learning rate, and dropout rate. All models except Models 15 and 17 (shown in italics) use an augmented training dataset; Models 15 and 17 use the same parameter values as Models 14 and 16, respectively, but with augmented training data. Model 6 (marked with **) is overall the best model; these predictions were used to make the maps in Fig.s 9–12. Predictions from Models 6, 7, 9, 16 and 17 (marked with *) were used to calculate the annual crevassed area from 2015-2024 (Fig. 15).*

Model	Epoch	Optimizer	Default learning rate	Testing learning rate	Epsilon/ Momentum	Dropout rate	Evaluation Metrics (%)			
							Mean IoU	IoU (Crevasse)	Accuracy	Loss
1	20	SGD	0.01	0.03	m=0.1	0.5	67.54	36.9	84.50	46.56
2	30	SGD	0.01	0.03	m=0.1	0.3	70.2	43.6	86.28	40.65
3	30	SGD	0.01	0.05	m=0.1	0.2	76.25	60.2	85.85	41.29
4	400	SGD	0.01	0.05	m=0.1	0.1	82.2	73	90.06	25.77
5	600	SGD	0.01	0.06	m=0.2	0.06	82.91	73.97	90.32	24.51
6**	900	SGD	0.01	0.06	m=0.2	0.1	83.15	74.77	90.56	23.88
7*	1000	SGD	0.01	0.07	m=0.2	0.08	82.7	74	91.44	20.79
8	1000	SGD	0.01	0.07	m=0.1	0.06	82.6	73.6	91.28	20.65
9*	1500	SGD	0.01	0.07	m=0.2	0.08	82.33	72.9	93.42	15.33
10	1000	RMS Prop	0.001	0.005	ε=0.01, m =0.3	0.08	82.13	72.4	90.93	21.43
11	20	Adam	0.001	0.003	ε=0.01	0.4	77.76	63.2	85.78	44.86
12	20	Adam	0.001	0.003	ε=0.01	0.5	68.76	39.9	85.29	45.06
13	30	Adam	0.001	0.001	ε=0.01	0.2	75.83	62.2	86.32	41.86
14	40	Adam	0.001	0.005	ε=0.01	0.4	26.56	0	70.53	98.61
15	*40*	*Adam*	*0.001*	*0.005*	*ε=0.01*	*0.4*	*69.62*	*42.2*	*86.45*	*39.51*
16*	700	Adam	0.001	0.002	ε=0.01	0.04	82.83	72.8	93.68	15.81
*17**	*700*	*Adam*	*0.001*	*0.002*	*ε=0.01*	*0.04*	*82.5*	*73.2*	*90.85*	*22.50*
18	700	Adam	0.001	0.007	ε=0.02	0.05	79.98	66.4	90.09	19.12

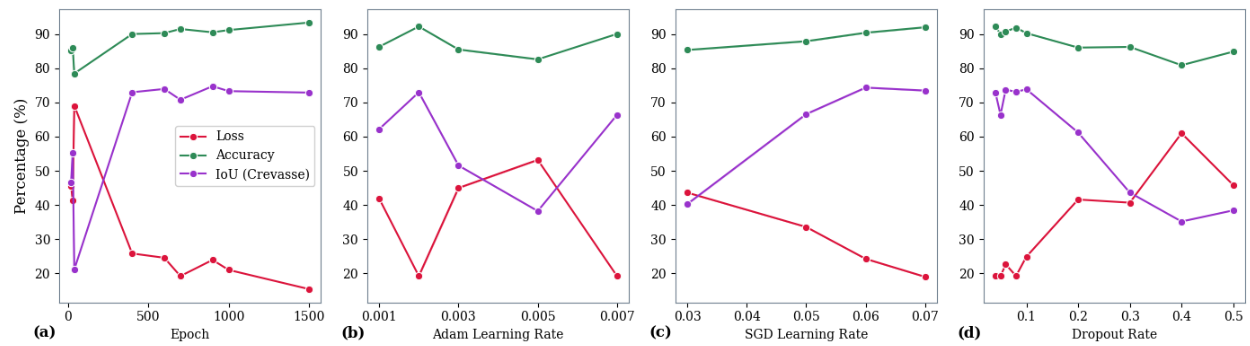

Figure S2: Model performance graphs as a function of parameter value choice. Panels show the percentage of loss (red), accuracy (green) and crevasse-class IoU (purple) versus a) number of epochs, b) learning rate for Adam optimizer, c) learning rate for SGD optimizer, and d) dropout rate.

We highlight model performance on non-augmented training datasets in runs 14 and 16. All other runs were models trained on a manually augmented training dataset. We found that the minor amount of data augmentation we inserted played a significant role during the early stages of model training and helped the model converge better at the end of the number of epochs. This is visible in run 14 versus run 15, where the model with the augmented dataset achieved a training loss of 39%, much lower than that of the model with non-augmented dataset, which achieved 98.6% loss and identified essentially no features of the crevasse field class. Interestingly, run 16 demonstrates that for longer training epochs (700 epochs), the non-augmented model's performance becomes comparable to those trained with augmented datasets over much shorter runs (40 epochs). For non-augmented models, we found that the Adam optimizer achieved the fastest model convergence among optimizers.

Next, we investigated the impact of different optimizers (Adam, SGD and RMSProp) and learning rates. The Adam optimizer performed best with smaller learning rates (values 0.001–0.007), while the SGD optimizer converged better with larger learning rates (values 0.01–0.07). While RMSProp achieved convergence with smaller learning rates similar to Adam, it introduced additional complexity due to its momentum and epsilon parameters. Both Adam and SGD, when used with their optimal learning rates, yielded the best performance overall. All of the optimizer functions reach their best model convergence with dropout rates ≤0.1.

As illustrated in Figure S2, model training performance varies with different hyperparameter settings. However, achieving an optimal model requires careful exploration and fine-tuning of these parameters. Simply selecting the values from Figure S2 that yield the highest accuracy and IoU and the lowest loss might not result in the best overall model. Instead, the key lies in finding a combination that optimizes all output metrics simultaneously. While monitoring accuracy, loss, and the mean IoU score, we prioritized the highest crevasse IoU score for final model selection. Although several models exhibited similar accuracy and loss ranges, Model 6 emerged as the best performer with a crevasse IoU score of 75% and a mean IoU score of 83%.

Finally, the architecture of the model, including the number of layers and feature maps, significantly influences its ability to detect all the features identified in the ground truth labels. A three-layered model achieved optimal performance when initialized to contain 16, 32, and 64 feature maps throughout the layers. This configuration allows the model to progressively learn more complex features, starting with simple edges in the first layer to more intricate crevasse field patterns in subsequent layers. However, increasing the number of feature maps beyond 64 led to a decline in detection accuracy. This suggests the effects of overfitting, where the model merely memorizes or replicates training data specifics instead of learning generalized features.

S3. Pathways to improve the usability of SAR imagery for crevasse detection

Our model sensitivity tests (Supplementary Section 1–2) uncovered a specific weakness of SAR-based techniques. SAR-based imagery produces a type of multiplicative noise called speckling, which causes problems with image classification. This underscores the need for robust speckle noise removal techniques. The frequent time-repeats of Sentinel-1 acquisitions (6–12 days) allow us to use a temporal median to reduce noise (Supplementary Section 1). However, in cases when only a single image is available, spatial filters such as Gaussian, spatial median, and spatial mean filters are commonly used for noise reduction (Coady and others, 2019). These filters essentially replace speckle noise with blurred noise (Yang and others, 2016). To date, denoising filters such as Lee, Kuan, Frost, and non-local means are the state-of-the-art methods for removing speckling (Bianco and others, 2018; Khan and Altalbe, 2022). These methods reduce speckle to variable degrees while retaining the main features of a speckled image. Zhao and others (2022) used probabilistic patch-based filtering, an extension of non-local means, to filter speckle noise and enhance the linear features of crevasses in Antarctica. Surawey-Stepney and others (2023) used parallel structure filtering to identify wide crevasses in Antarctica. For crevasses on Antarctic ice shelves, which have typical widths on the order of 100 m to 1 km and typical lengths on the order of 1 to 10 km (Surawy-Stepney and others, 2023), speckle noise blurred across five to ten Sentinel-1 pixels (50–100 m) does not problematically obscure this signal. However, for the narrower and shorter Greenland crevasses we study, blurring over this spatial scale would remove the signal we seek. Thus, another way to denoise individual images is needed.

CNN-based methods are being developed for more efficient speckle noise removal, but these supervised deep-learning methods still require noiseless image masks as ground truth labels for training (Passah and others, 2021). Such noiseless masks do not exist for Sentinel-1 data over ice sheets. To bridge this gap, we envision that Generative Adversarial Networks (GANs) could be combined with CNN models to produce denoised image outputs. GAN models are trained to produce synthetic data (Goodfellow and others, 2020). In this case, a GAN model would be trained on artificially added noise on relatively clear SAR images (or images like the ones we use here images that have effectively been despeckled using a temporal median, for example). Then the model would produce a despeckled SAR image when given an input with speckle noise.

Future efforts should aim for a combined GAN–CNN workflow to successfully despeckle SAR imagery for Greenland crevasses and achieve higher accuracy in crevasse detection.

References

Bianco V and 8 others (2018) Strategies for reducing speckle noise in digital holography. *Light Sci Appl* 7, 48. https://doi.org/10.1038/s41377-018-0050-9

Coady J, O'Riordan A, Dooly G, Newe T and Toal D (2019) An overview of popular digital image processing filtering operations. In *2019 13th International conference on sensing technology (ICST)* (pp. 1-5). IEEE. https://doi.org/10.1109/ICST46873.2019.9047683

Goodfellow I and 7 others (2020) Generative adversarial networks. *Communications of the ACM*, *63*(11), pp.139-144. https://doi.org/10.48550/arXiv.1406.2661

Khan MN and Altalbe A (2022) Experimental evaluation of filters used for removing speckle noise and enhancing ultrasound image quality. *Biomedical Signal Processing and Control*, *73*, 103399. https://doi.org/10.1016/j.bspc.2021.103399

Passah A, Amitab K and Kandar D (2021) SAR image despeckling using deep CNN. *IET Image Processing*, *15*(6), 1285-1297. https://doi.org/10.1049/ipr2.12104

Surawy-Stepney T, Hogg AE, Cornford SL and Hogg DC (2023) *Mapping Antarctic Crevasses and their Evolution with Deep Learning Applied to Satellite Radar Imagery*. Copernicus GmbH. Retrieved from http://dx.doi.org/10.5194/tc-2023-42

Yang J and 6 others (2016) Local statistics and non-local mean filter for speckle noise reduction in medical ultrasound image. *Neurocomputing*, *195*, 88-95. https://doi.org/10.1016/j.neucom.2015.05.140

Zhao J, Liang S, Li X, Duan Y and Liang L (2022) Detection of Surface Crevasses over Antarctic Ice Shelves Using SAR Imagery and Deep Learning Method. *Remote Sensing*, *14*(3), 487. https://doi.org/10.3390/rs14030487